JUNE 1982 LRP 209/82

EXPERIMENTS ON POTENTIAL GRADIENTS IN A CURRENT CARRYING PLASMA

PART I : POTENTIAL STRUCTURES

M. Guyot and Ch. Hollenstein

Experiments on potential gradients in a current carrying plasma. Part I : Potential Structures

M. Guyot and Ch. Hollenstein

Centre de Recherches en Physique des Plasmas
Association Euratom - Confédération Suisse
Ecole Polytechnique Fédérale de Lausanne
CH-1007 Lausanne / Switzerland

ABSTRACT

In a current carrying plasma with $v_d < v_{te}$, constant potential gradients and strong localized potential jumps have been observed under different experimental conditions. One or more potential jumps with $e\Phi/kTe \approx 10\text{-}12$ and a typical width of 10-15 cm may exist. Measurements of the electron distribution function show the presence of a beam on the high potential side. This electron beam is thermalized within 10-20 cm leading to strong localized electron heating. Ion heating as well as peaked anomalous resistivity are found within the jump.

In the case of a constant potential gradient, ion and electron heating has been observed. However no electron beam could be detected. The resistivity is anomalous for this case also.

I INTRODUCTION

In recent years localized potential gradients have been observed in laboratory plasmas [1-18] as well as in the magnetosphere [19,20]. These large potential steps are thought to play an important role in cosmic plasma physics. They are presumed to be responsible for the acceleration of the fast electrons detected in the ionosphere [21,22]. They may also be involved in the physics of solar flares [23] and related phenomena [24]. A number of theories [25-39] have been advanced to explain these potential gradients referred to as double layers, potential jumps or potential steps.

Double layers, the term first coined by Langmuir, consist basically of two space-charge layers of oppositely charged particles. The typical width of these layers is a few 10 Debye lengths. The potential drop across the double layer is of the order of a few times $e\Phi/kT_e$. The occurence of this phenomenon has been demonstrated by BGK theory [38] and numerical simulations [30,34].

A variety of experimental conditions induce potential steps [1-4,6,7,14,18b]. Essentially two types of fluctuations are observed associated with these layers. The fluctuations in the range of the electron plasma frequency are induced by the electron beam caused by the potential step [2,10]. The low frequency fluctuations are identified as the Buneman instability induced by the electron drift [27]. This is in agreement with the theory [38] which predicts that double layers in a current carrying plasma can only be formed if the electron drift velocity v_{de} exceeds the electron thermal velocity.

Theoretical considerations [37] and numerical simulations [36] indicate that this condition on the electron drift speed may not be necessary for the existence of a potential step. Sato et al. [36,37] have proposed that the current-driven ion acoustic instability leads to the build up of potential steps. The anomalous resistivity generated by the instability is assumed to be the layer generating mechanism provided the system is sufficiently long. Even without currents potential steps may be obtained [39].

In a previous paper [40] we reported the observation of potential jumps in a current carrying plasma. Under our experimental conditions the electron drift velocity always remained much smaller than the electron thermal velocity. ($v_{de} < 0.2\ v_{te}$). The appearance of one or even more stationary potential jumps was shown. The plasma was observed to be strongly turbulent within the steps.

In the present paper we wish to report a systematic exploration of potential jumps. In addition, we present experimental conditions in which no step occurs despite a large potential applied to the plasma. Strong ion acoustic turbulence and anomalous resistivity are also observed in that case. However no clear indication of the formation of the so-called double layers is seen. From our experience a wide variety of potential shapes can exist in a plasma and a great number of different mechanisms may be responsible for their formation. This would constitute a large field for further investigations in non-linear plasma physics.

Section II describes the experimental setup. Section III reviews the different diagnostic devices used to investigate the plasma. The experimental results are described in Section IV.

II EXPERIMENTAL DEVICE

The measurements described later were all made in a cylindrical stainless steel vessel whose length and diameter are 300 cm and 22 cm respectively (Fig. 1). The outside of the vessel is covered with permanent magnets. Eight coils are placed along the metallic tube which produce a constant magnetic field of 25 Gauss.

Each end of this tube is terminated by a plasma source, which is separated from the tube by a grid with a transparency of 74 %. The tube, the grids and the sources are electrically insulated and can be separately polarized. Each source contains 10 tungsten filaments which can be heated to emit electrons and which are negatively biased at -60V with respect to the envelope of the source. The sources are normally operated with the grids positively biased with respect to their envelope. One grid was connected to the tube which was grounded, the other was polarized positively at different voltages V_g, with respect to the tube. The two sources will be referred to as the cathode and anode. The device is usually filled with argon at a pressure of 4×10^{-4} Torr.

If V_g = 0V, a uniform plasma is created in the tube. Its electron density, and electron and ion temperatures are $n_e = 2 \times 10^9 cm^{-3}$, T_e = 1.2eV and T_i = 0.2eV, respectively.

The experiment was performed under two different conditions. In the triple plasma case, both sources operate identically. For positive grid voltages a current flows and an electric field is established within the plasma. The plasma potential, is usually non uniform, exhibiting steps. At the same time large electrostatic fluctuations appear.

These phenomena have been analyzed in detail and will be described in Section IV. In some experiments the filaments of the cathode source were not heated. We refer to this condition as the double plasma case.

III MEASUREMENT TECHNIQUES

The electron density n_e, the electron temperature T_e and the low frequency density fluctuation $\delta n/n$ were measured using a cylindrical Langmuir probe of diameter 0.3 mm and length 5 mm.

The plasma potential was measured using a hot emitting probe with a hot tungsten filament of 0.08 mm diameter. The heating current of the hot probe was pulsed and a boxcar integrator was used to sample the probe current during the off-cycle of the heating voltage [41]. The accuracy of this measurement is estimated to be of the order of $\Delta V_p \approx k_B T_f/e$ where T_f is the filament temperature. With this type of probe, axial and radial potential maps were established.

In current carrying plasmas the measurement of the electron drift velocity is critical. For this measurement the method of rotating Langmuir probes was chosen [42].

The upstream and downstream electron distribution functions were measured using two flat one-sided Langmuir probes (diameter = 2.0 mm) fitted back to back. The distribution functions are obtained from the differentiated Langmuir characteristic.The ion temperature T_i was determined using a one-grid electrostatic energy analyzer. Its resolution is estimated to be better than 0.1 eV.

Special care has been taken for the measurement of the noise frequency spectra. Capacitive probes appear to give the most reliable values [43] and were used for both high and low frequency spectra. A detailed study of the instabilities associated with the potential structure has been made and are published in a companion paper [43].

IV EXPERIMENTAL RESULTS

The axial potential profiles exhibit completely different shapes for the triple and double plasma cases (Figs. 2 and 3). In the former case, the plasma potential reveals one or more stationary potential jumps as the anode grid voltage is increased (Fig. 2). The formation of a potential jump is observed for grid voltages higher than about 5V. The heights of these jumps are of the order of $e\Phi/kT_e \approx 10$ and their width is typically 300 - 500 λ_{De}. For a wide range of

experimental conditions no higher steps could be observed. Instead, the appearance of a second or third jump has been seen with all its accompanying phenomena. In the double plasma case, however, no potential jumps have been observed, a nearly constant potential gradient being established all along the central section of the tube (Fig. 3).

A. Dependance on the grid voltage V_g

1. Triple Plasma Case

For V_g = 0V the plasma potential and the electron temperature are constant all along the tube. The normalized turbulent wave energy $W/nT_e \approx (\delta n/n)^2$ is found to be less than 2.5×10^{-5}. The electron density profile is flat in the centre and shows an increase towards the sources, due to plasma injection.

However, even at small grid voltages (Fig. 4), a localized stationary potential gradient appears near the polarized grid, with an associated density dip. A simultaneous local increase in the low frequency noise and local electron heating are observed. At V_g = 10 V, the measurements show the same tendencies but in a more pronounced way (Fig. 5). Further development of the potential jump with increasing V_g is shown in Fig. 6. Here, the most striking effect is the appearance of a second structure, some 5000 λ_{De} upstream from the grid. This new jump then becomes larger with increasing grid

voltage (Fig. 7). At the same time, a second fluctuation peak emerges. On the high potential side of this new step another local electron heating peak is observed, and a new dip appears in the electron density (Fig. 7). For the highest grid voltage used (V_g = 50 V), three potential jumps are present, (Fig. 8). Each of these are accompanied by the associated phenomena described above. From these measurements, we see that a localized stationary potential gradient is always accompanied by the same set of phenomena. The three main features are : i) a pronounced density dip ($\sim$40 %) at the jump location, ii) the appearance of a low frequency fluctuation peak at the low potential side of the jump, iii) strong f_{pi} fluctuations and a strong local electron heating at the top of the jump and electron heating in the low potential region. We therefore concentrate our investigation on one case, namely V_g = 20 V. For this value of grid voltage, a single fully-developed localized potential jump exists.

The following study is then restricted to the V_g = 20 V case which we shall discuss in more detail (Figs. 9 and 10). For this case, the height $e\Phi/kT_e$ and the width of the potential jump are 12 and 300 - 600 λ_{De}, respectively. The electric field reaches a maximum value of about 1 V/cm. This field corresponds to a charge separation of about 0.1 % of the unperturbed density. The maximum of the field and the location of the two oppositely charged layers lie exactly within the observed density dip. The low frequency noise could be identified as ion acoustic fluctuations. An electron beam was observed on the high potential side of the step, inducing high frequency fluctuations around f_{pe}. The peaks of the electron temperature and high frequency

noise occur at the same location, indicating that these local increases are due to the thermalization of the electron beam. The upstream and downstream measurements of the ion temperature show ion heating on the low potential side of the jump (Fig. 10). This heating may be due to the thermalization of the detected ion beam associated with the potential drop. Measurements of the electron drift velocity are also presented in Fig. 10. They show that the electron drift velocity remains well below the electron thermal velocity, reaching a maximum value of about 0.2 x v_{te} [$v_{te} = \left(\frac{8}{\pi} \cdot \frac{k_B \cdot T_e}{m}\right)^{1/2}$]. This fact is supported by the frequency spectra, which lies below f_{pi}. No indication of the Buneman instability was found [43]. On this point, our experiment differs essentially from all the double layer experiments where v_{de} exceeds v_{te}.

Using both the computed electric field and the electron drift velocity measurements, an effective collision frequency ν^* can be obtained. Figure 11 shows that anomalous resistivity exists. On the high potential side of the jump, the effective collision frequency has been found to reach values up to 100 times the classical value. Only 10 times the classical value has been observed on the low potential side. However, ν^* of about 700 times prevails within the jump. At this position the effective mean free path (λ = 1 - 2 cm) has been found to be much smaller than the width of the observed step (L = 10 - 15 cm).

2. Double Plasma Case

In this mode of operation, the behavior of the plasma potential differs from that in the triple plasma mode. For increasing grid voltages (Fig. 12), a potential gradient grows without any appearance of a step. The localized density fluctuation peak increases and moves towards the anode. Electron heating is observed without any localized peaking. The electron density shows no significant dips. For $V_g >$ 30 V (Fig. 13), a broadening of the density fluctuation peak is observed, and a second peak even appears (Fig. 14). The fluctuation level is comparable to that measured for the triple plasma case. No jumps in the potential profile are observed. However, a slight potential perturbation emerges in the region of the fluctuation peak. Neither an electron nor an ion beam could be detected for any value of V_g.

A detailed study of the double plasma case has been performed for V_g = 20 V. This allows a comparison between the physics involved in each case for the same grid voltage. Figs. 15 and 16 show the potential, electron density, low frequency fluctuation level and temperature profiles. The upstream and downstream ion temperatures agree within the measurement error. Ion heating is observed toward the cathode. The electron drift velocity, as in the triple plasma case, never exceeds the electron thermal velocity. The maximum value it reaches under these conditions is about the same as in the previous case. This is again in accordance with the observed instability, which

was identified as the ion acoustic instability. The effective collision frequency remains almost constant along the tube (Fig. 11). Its value reaches about 100 times the classical value ν_{cl}.

B. Distribution functions

In addition to the potential profile, the electron distribution is also of importance in the problem of potential gradients in current carrying plasmas. In the current free case (V_g = 0V) the measured electron distributions are symmetric and may be considered as Maxwellian at all positions along the axis of the device.

The electron distribution functions exhibit quite a different behavior for the double and the triple plasma cases. Figure 17 shows the plasma potential profile with the corresponding half distributions measured along the axis. The two halves of a distribution are labeled by the letters A and C. Letter A denotes the contribution from particles traveling from the anode side toward the cathode (positive velocities) while C is used for particles traveling in the opposite direction (negative velocities). The emergence of a strong electron beam clearly appears inside the jump. On the high potential side however, this beam disappears due to thermalization and non-linear effects. The beam energy is most likely dissipated into the strong high frequency ($\sim f_{pe}$) turbulence and particle heating observed inside this region. Furthermore, a difference in amplitude between A and C contributions is observed. The number of particles having negative velocities is larger than the number of particle traveling in

the opposite direction. Similar shapes of electron distributions were observed in numerical simulations [46]. Far away from the jump, the distributions look like those of the current-free case.

In the double plasma case (Fig. 18) the most remarkable aspect is the absence of any electron beam. As in the previous case the distributions are asymmetric. Measurements with an ion energy analyzer showed the presence of a strong ion beam on the low potential side of the jump. As for the electron distribution, anisotopic behavior is also found for the ion distribution.

C. Mapping of the plasma potential

The mapping of the plasma potential was done only for the triple plasma case. It was performed with a movable hot probe. The plasma diameter was scanned using probes with different probe lengths. Figure 19(a) shows the equipotential lines in the vertical plane containing the axis of the device. The radial potential profiles at several positions along the machine are shown in Fig. 19(b).

The radial profile near the anode grid (position I) is almost constant over the diameter. Approaching the potential jump (II), a large radial plasma potential gradient appears. The corresponding radial electric field component E_r is found to be as large as the longitudinal E-field component E_z. Near the tube axis, a dip in the plasma potential appears. At the bottom of the step (III), the same

behavior is observed. On the low potential side (IV), the profiles flatten and only a dip around the axis remains up to the end of the tube (V). These features are shown in Fig. 19(a) in a global picture. The shape of the observed potential cannot be considered as a U or V shaped layer as described by many authors [6,35]. The structure is two dimensional with a complicated internal fine structure. The most remarkable feature is the local penetration of equipotential lines far into the region near the cathode. These finger-like structures start at the jump, at mid radius, forming a potential hole on axis. The radial profiles of most parameters show a peaking within the region limited by these finger-like structures.

D. Radial profiles

In spite of the results from the plasma potential mapping, additional knowledge of the radial behavior of the basic plasma parameters is essential to obtain an understanding of the phenomena investigated.

The radial profiles for V_g = 20 V are shown in Fig. 20. These are measured on the low potential side of the device at a distance of 110 cm from the anode grid. Across the diameter, the electron temperature has a constant value of about 2.5 eV. The low frequency noise $\delta n/n$ is also constant. The density, however peaks on the axis at the location of the potential dip. Outside this region it remains constant up to about 6 cm on each side of the axis, which corresponds to the position of the equipotential finger-like structures.

The measurement of the electron beam energy on the axis is shown in Fig. 21(a). The solid line corresponds to the energy gained by electrons from the low potential side passing through the potential jump. A lock-in method was used to detect the electron population arriving on the high potential side. A modulation was applied to the cathode grid, with a frequency less than the frequencies of the ion acoustic instability. The modulated population was detected on the high potential side of the jump with a plane Langmuir probe. With this technique, we were able to detect selectively the electrons coming from the cathode side. It was found that the electrons arriving at the location of the probe were only those of the beam. The radial profile of the beam energy is presented in Fig. 21(c). The electron beam is detected only within a radius of 6 cm around the tube axis. The plasma outside of this region was identified, by the modulational method, as the low potential side plasma. This is in agreement with the electron temperature profile shown in Fig. 21(b). High electron temperature is observed only in the central region of the tube, due to the beam thermalization. At larger radial positions, the temperature agrees with that of the cathode side plasma. The electron density peaks in the same region (Fig. 21(d)).

V CONCLUSIONS

In a current carrying plasma with an electron drift velocity smaller than the electron thermal velocity, the formation of a strongly turbulent potential jump has be observed. Several potential

jumps were observed at larger values of the plasma current. Each of them shows the same physical phenomena. The low frequency ($\leq f_{pi}$) instability on the low potential side is identified as the ion acoustic instabiliy [43]. The ion beam induced by the potential jump is dissipated on the low potential side resulting in ion heating. On the low potential side far away from the jump, ion acoustic turbulence is excited by the electron drift. The high frequency ($\sim f_{pe}$) instability is caused by the electron beam formed by the jump. This beam is dissipated by quasi-linear effects on the high potential side, therefore leading to local electron heating.

In addition, a potential structure with a nearly constant gradient all along the tube could be generated. As in the previous cases, the plasma is found to be locally highly turbulent. Anomalous resistivity also exists under these conditions. However, no evidence for a steepening in the potential gradient could be detected. The electron beam does not appear and therefore no high frequency turbulence has been found.

We do not know of any theory that could explain all of our observations in a consistent way. However, several theories can be excluded. As was shown in detail, the plasma is in a highly turbulent state. Therefore any laminar double layer theory must be rejected. In addition, a BGK-like model was investigated in order to show the existence of stable stationary potential steps. This theory fails to explain our observation of potential steps in a current carrying plasma with $v_d < v_{te}$. However, potential jumps have been observed

in recent numerical simulation [36,46]. To the extent to which a comparison can be made, similarities are found between our experiment and these simulations. The main points of agreement are: i) the existence of one or more potential jumps in a current carrying plasma with $v_d < v_{te}$; ii) the presence of ion acoustic turbulence; and iii) similar features for the upstream electron distribution.

The experimental results may be simply described as the collision of two plasmas with different plasma potentials. However, the question remains as to how such a stable stationary potential can be maintained. Additional experimental and theoretical work must be performed in order to clarify the problem of large potential gradients in current carrying plasmas.

ACKNOWLEDGMENTS

The authors wish to thank Professor E.S. Weibel, Dr. M.Q. Tran, Dr. J. Vaclavik, and Dr. K. Appert for many fruitful discussions.

This work was supported by the Swiss National Science Fondation, the Ecole Polytechnique Fédérale and by EURATOM.

REFERENCES

1) B.H. Quon and A.Y. Wong, Phys. Rev. Lett. 37, 1393 (1976)

2) P. Leung, A.Y. Wong, and B.H. Quon, Phys. Fluids 23, 992 (1980)

3) P. Coakley, N. Hershkowitz, R. Hubbard, and G. Joyce, Phys. Rev. Lett. 40, 230 (1978)

4) P. Coakley and N. Hershkowitz, Phys. Fluids 22, 1171 (1979)

5) P. Coakley, L. Johnson, and N. Herzkowitz, Phys. Lett. 7017, 425 (1979)

6) R.L. Stenzel, M. Ooyama, and Y. Nakamura, Phys. Rev. Lett. 45, 1498 (1980)

7) S. Jizuka, K. Saeki, N. Sato, and Y. Hatta, Phys. Rev. Lett. 43, 1404 (1979)

8) K. Saeki, S. Jizuka, and N. Sato, Phys. Rev. Lett. 45, 1853 (1980)

9) S. Torvén and D. Andersson, Appl. Phys. 12, 717 (1979)

10) S. Torvén and L. Lindberg, Appl. Phys. 13, 2285 (1980)

11) S. Torvén and M. Babic, in Proceedings of the 12th International Conference on Phenomena in Ionized Gases 1975, edited by J.G. Hölscher and D.C. Schram, (American Elsevier, New York, 1975), p.124

12) J.S. Levine and F.W. Crawford, J. Plasma Phys. 24, 359 (1980)

13) J.S. Levine, F.W. Crawford, and D.B. Ilic, Phys. Lett. 65A, 27 (1978)

14) F.W. Crawford and I.L. Freeston, in 6th International Conference on Phenomena in Ionized Gases, edited by P. Hubert and E. Crémien-Alcan, (EURATOM-CEA, Paris, 1963), Tome I, p. 461

15) M.J. Schönhuber, Z. Angew. Phys. 15, 545 (1963)

16) E.I. Lutsenko, N.D. Sereda, and L.M. Kontsevoi, Zh. Tekh. Fiz. 45, 789 (1975) [Sov. Phys. Tech. Phys 20, 498 (1976)]

17) N. Singh, R. Kist, H. Thiemann, and L.P.Block, Plasma Phys. 22, 695 (1980)

18) a) S. Torvén in Wave Instabilities in Space, edited by P.J. Palmadesso and K. Papadopoulos, Plasma Astrophysics and Space Science Library (D. Reidel, Dordecht, 1979), Vol. 74, p. 109

b) F.W. Crawford, J.S. Levine, and P.B. Ilic, in edited by P.J. Palmadesso and K. Papadopoulos), Plasmas Astrophysics and Space Science Library (D. Reidel, Dordecht, 1979), Vol. 74, p. 129

19) E.M. Wescott, H.C. Stenbaek-Nielsen, T.J. Hallinan, T.N. Davis, and H.M. Peek, J. Geophys. Res 81, 4495 (1976)

20) F.S. Mozer, C.W. Carlson, M.K. Hudson, R.B. Tobert, B. Parady, J. Yaltean, and M.C. Kelley, Phys. Rev. Lett. 38, 292 (1977)

21) H. Alfvén, Tellus 10, 104 (1958)

22) R.D. Albert and R.P.J. Lindstrom, Science 170, 1398 (1970)

23) H. Alfvén and P. Carlqvist, Solar Phys. 1, 220 (1967)

24) R.A. Smith and C.K. Goertz, J. Geophys. Res. 83, 2617 (1978)

25) P. Carlqvist, Cosmic Electrodyn. 3, 377 (1972)

26) L.P. Block, Cosmic Electrodyn. 3. 349 (1972)

27) L.P. Block, B. Hultqvist, and L. Stenflo, editors Physics of the Hot Plasma in the Magnetosphere, (Plenum, New York, 1975)

28) L.P. Block, Astrophys. Space Sci. 55, 59 (1978)

29) G. Knorr and C.K. Goertz, Astrophys. Space Sci. 31, 209 (1974)

30) C.K.Goertz and G. Joyce, Astrophys. Space Sci. 32. 165 (1975)

31) G. Joyce and R.F. Hubbard, J. Plasma Phys. 20, 391 (1978)

32) H. Schamel and S. Bujarbarna, (to be published)

33) J.S. Levine and F.W. Crawford, J. Plasma Phys. 23, 223 (1980)

34) J.S. DeGroot, C. Barnes, A.E. Walstead, and O. Buneman, Phys. Rev. Lett. 38, 1283 (1977)

35) J.S. Wagner, T. Tajima, J.R. Kan, J.N. Leboeuf, S.I. Akasofu, and J.M. Dawson, Phys. Rev. Lett. 45, 803 (1980)

36) T.Sato and H. Okuda, Phys. Rev. Lett. 44, 740 (1980)

37) A. Hasegawa and T. Sato Phys. Fluids 25, 632 (1982)

38) P. Carlqvist in Wave Instabilities in Space, edited by P.J. Palmadesso and K. Papadopoulos, (D. Reidel, Dordecht, 1979), Vol. 74, p.83

39) F.W. Perkins and Y.C. Sun, Phys. Rev. Lett. 46, 115 (1981)

40) Ch. Hollenstein, M. Guyot, and E.S. Weibel, Phys. Rev. Lett. 45, 2110 (1980)

41) J.R. Smith, N. Hertzkowitz, and P. Coakley, Rev. Sci. Instrum. 50, 210 (1979)

42) A. Hirose, I. Alexeff, W.D. Jones, S.T. Kush, and K.E. Lonngren, Phys. Rev. Lett. 25, 1563 (1970)

43) Ch. Hollenstein, and M. Guyot, Phys. Fluids, (Part II)

44) B.B. Katomtsev, Plasma Turbulence (Academic, New York, 1965)

45) R.Z. Sagdeev, Rev. Mod. Phys. 51, 1 (1979)

46) T. Sato and H. Okuda, J. Geophys. Res., 86, 3357 (1981)

Figure Caption

Fig. 1. Schematic of the long triple plasma device.

Fig. 2. Steady-state plasma potential versus position as a function of the grid bias V_g. (Triple plasma). The biased grid is located at $z = 0$

Fig. 3. Steady-state plasma potential versus position as a function of the bias V_g (double plasma). The biased grid is located at $z = 0$

Fig. 4. Plasma potential V_p, electron density n_e, electron temperature T_e, and low frequency fluctuation level $\delta n/n$ versus position for $V_g = 5V$ (triple plasma). The biased grid is located at $z = 0$

Fig. 5. Plasma potential V_p, electron density n_e, electron temperature T_e, and low frequency fluctuation level $\delta n/n$ versus position for $V_g = 10V$ (triple plasma). The biased grid is located at $z = 0$

Fig. 6. Plasma potential V_p, electron density n_e, electron temperature T_e, and low frequency fluctuation level $\delta n/n$ versus position for $V_g = 30V$ (triple Plasma). The biased grid is located at $z = 0$

Fig. 7. Plasma potential V_p, electron density n_e, electron temperature T_e, and low frequency fluctuation level $\delta n/n$ versus position for V_g = 40V (triple plasma). The biased grid is located at z = 0

Fig. 8. Plasma potential V_p, electron density n_e, electron temperature T_e, and low frequency fluctuations level $\delta n/n$ versus position for V_g = 50V (triple plasma). The biased grid is located at z = 0.

Fig. 9. Plasma potential V_p, electron density n_e, and low frequency fluctuation level $\delta n/n$ versus position for V_g = 20V (triple plasma). The biased grid is located at z = 0

Fig.10. The electron temperature T_e, the ion temperature T_i and the normalized electron drift velocity v_d/v_{te} $\left[v_{te} = \left(\frac{8}{\pi} \cdot \frac{k_B T_e}{m}\right)^{1/2}\right]$ versus position for V_g = 20V (triple plasma). The biased grid is located at the position z = 0

Fig.11. The effective collision frequency ν^* versus position.
a) double plasma; b) triple Plasma.

Fig.12. Plasma potential V_p, electron density n_e, electron temperature T_e, and low frequency fluctuation level $\delta n/n$ versus position for V_g = 15V (double plasma mode). The biased grid is located at z = 0.

Fig.13. Plasma potential V_p, electron density n_e, electron temperature T_e, and low frequency fluctuation level $\delta n/n$ versus position for V_g = 30 V (double plasma). The biased grid is located at z = 0.

Fig.14. Plasma potential V_p, electron density n_e, electron temperature T_e, and low frequency fluctuation level $\delta n/n$ versus position for V_g = 40V (double plasma). The biased grid is located at z = 0.

Fig.15. Plasma potential V_p, electron density n_e and low frequency fluctuation level $\delta n/n$ versus position for V_g = 20V (double plasma). The biased grid is located at z = 0.

Fig.16. Electron temperature T_e, the temperature T_i and normalized electron drift velocity v_d/v_{te} $\left[v_{te} = \left(\frac{8}{\pi} \cdot \frac{k_B T_e}{m} \right)^{1/2} \right]$ versus position for V_g = 20V (double plasma). The biased grid is located at z = 0.

Fig.17. Measurements of the electron distribution function f(E) at different positions from the biased grid for V_g = 20V (triple plasma). Shown are the electronically differentiated Langmuir traces for both upstream (C) and downstream (A) probe orientations.

Fig.18. Measurements of the electron distribution function f(E) at different positions from te biased grid for V_g = 20V (double plasma). Shown are the electronically differential Langmuir traces for both upstream (C) and downstream (A) probe orientations.

Fig.19. Plasma potential in the (r, z) plane.

a) Mapping of plasma potential for V_g = 20V (triple plasma)

b) Radial profiles of measured plasma potential at the position indicated by I, II, III, IV, V.

Fig.20. Radial profile of the electron temperature, the electron density and the low frequency fluctuation level $\delta n/n$ for V_g = 20V, at 185 cm from the biased grid. This position is on the low potential side of the jump.

Fig.21. Radial profils on the high potential side.

a) Electron beam energy versus position for V_g = 20V. The line corresponds to the potential difference between low and high potential side on the jump.

b) Radial profile of the electron temperature T_e profile on the high potential side (z = 41 cm) for V_g = 20V.

c) Radial profile of the electron beam energy on the high potential side of the jump (Z = 41 cm) for V_g = 20V.

d) Radial profile of the electron density on the high potential side of the jump.

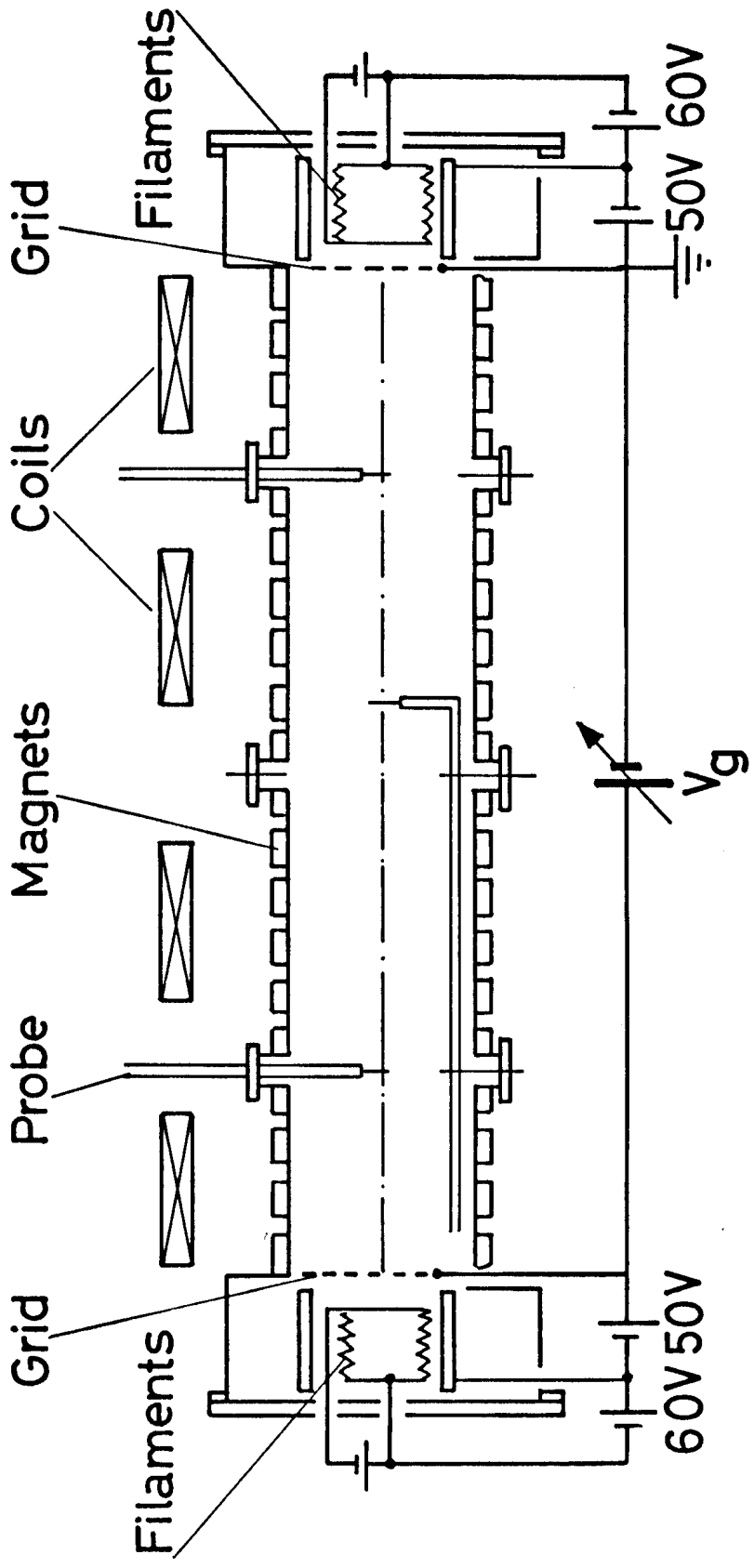
Filaments
Grid
Coils
Magnets
Probe
Grid
Filaments
60V
50V
V_g
60V
50V

fig. 1

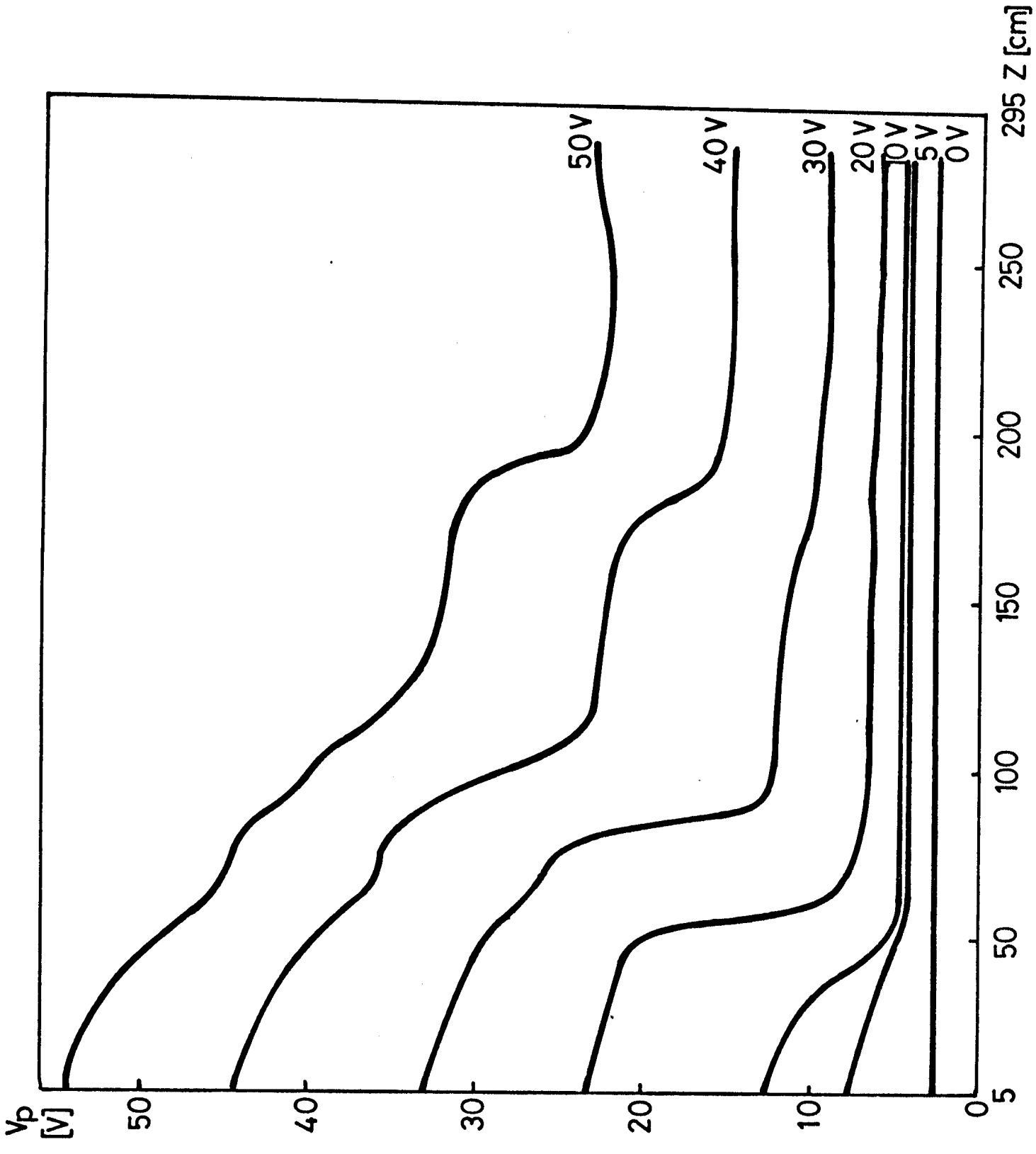
50 V
40 V
30 V
20 V
10 V
5 V
0 V
V_p [V]
50
40
30
20
10
0
5
50
100
150
200
250
295 Z [cm]

fig. 2

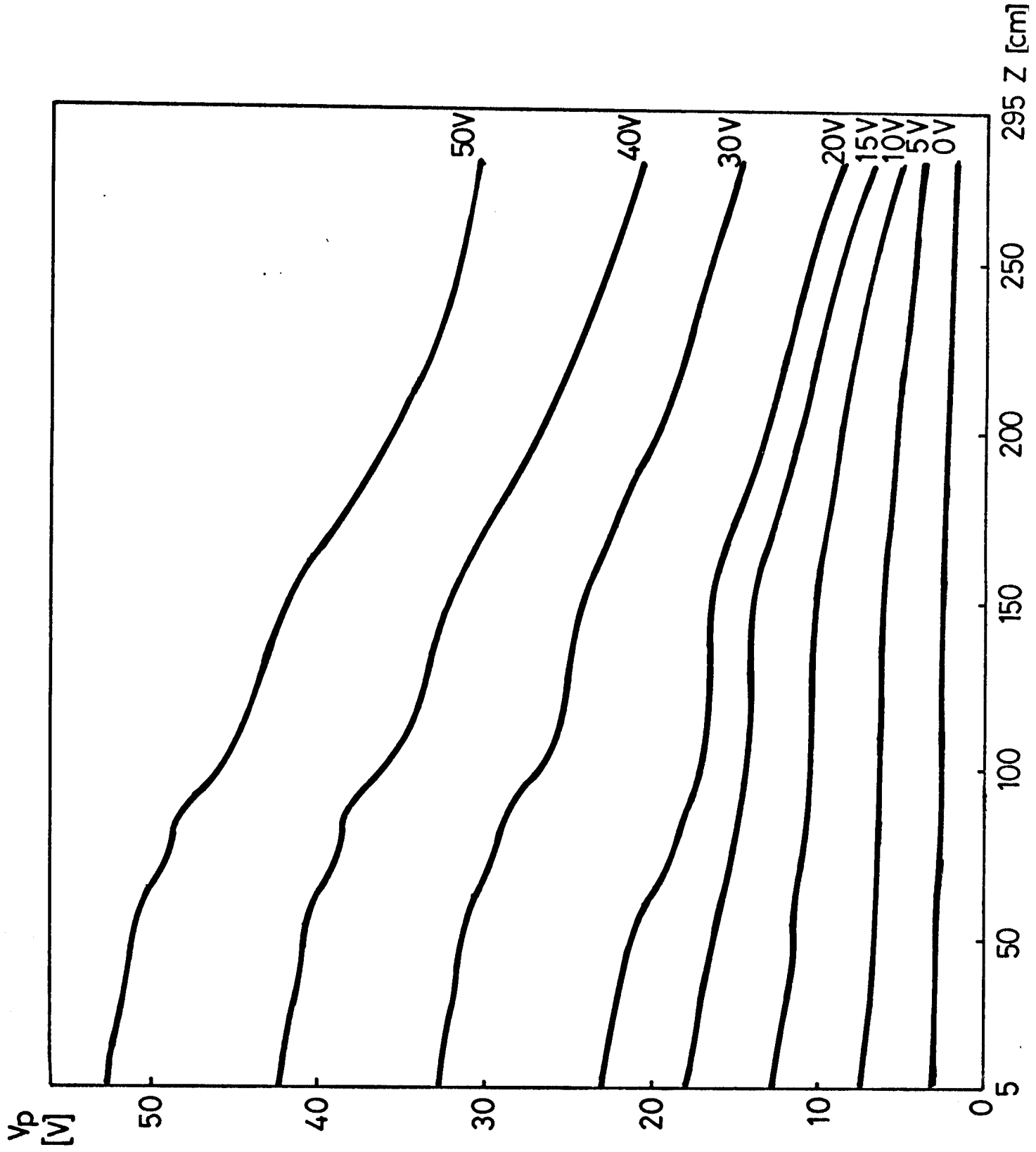
50V
40V
30V
20V
15V
10V
5V
0V
Vp [V]
0
10
20
30
40
50
5
50
100
150
200
250
295 Z [cm]

fig. 3

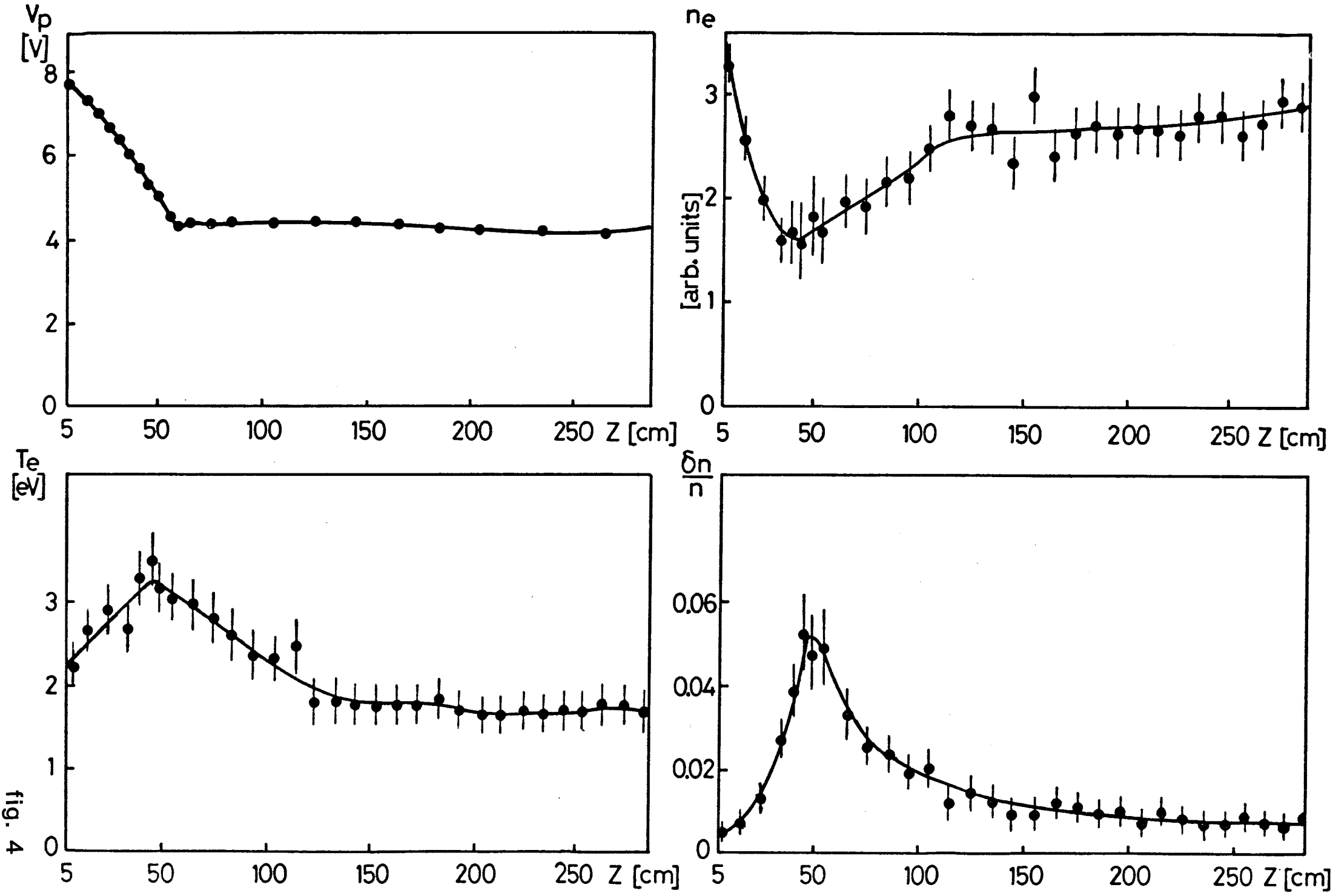
V_p [V]
8
6
4
2
0
5
50
100
150
200
250 Z [cm]
n_e
[arb. units]
3
2
1
0
5
50
100
150
200
250 Z [cm]
Te [eV]
3
2
1
0
5
50
100
150
200
250 Z [cm]
$\frac{\delta n}{n}$
0.06
0.04
0.02
0
5
50
100
150
200
250 Z [cm]

fig. 4

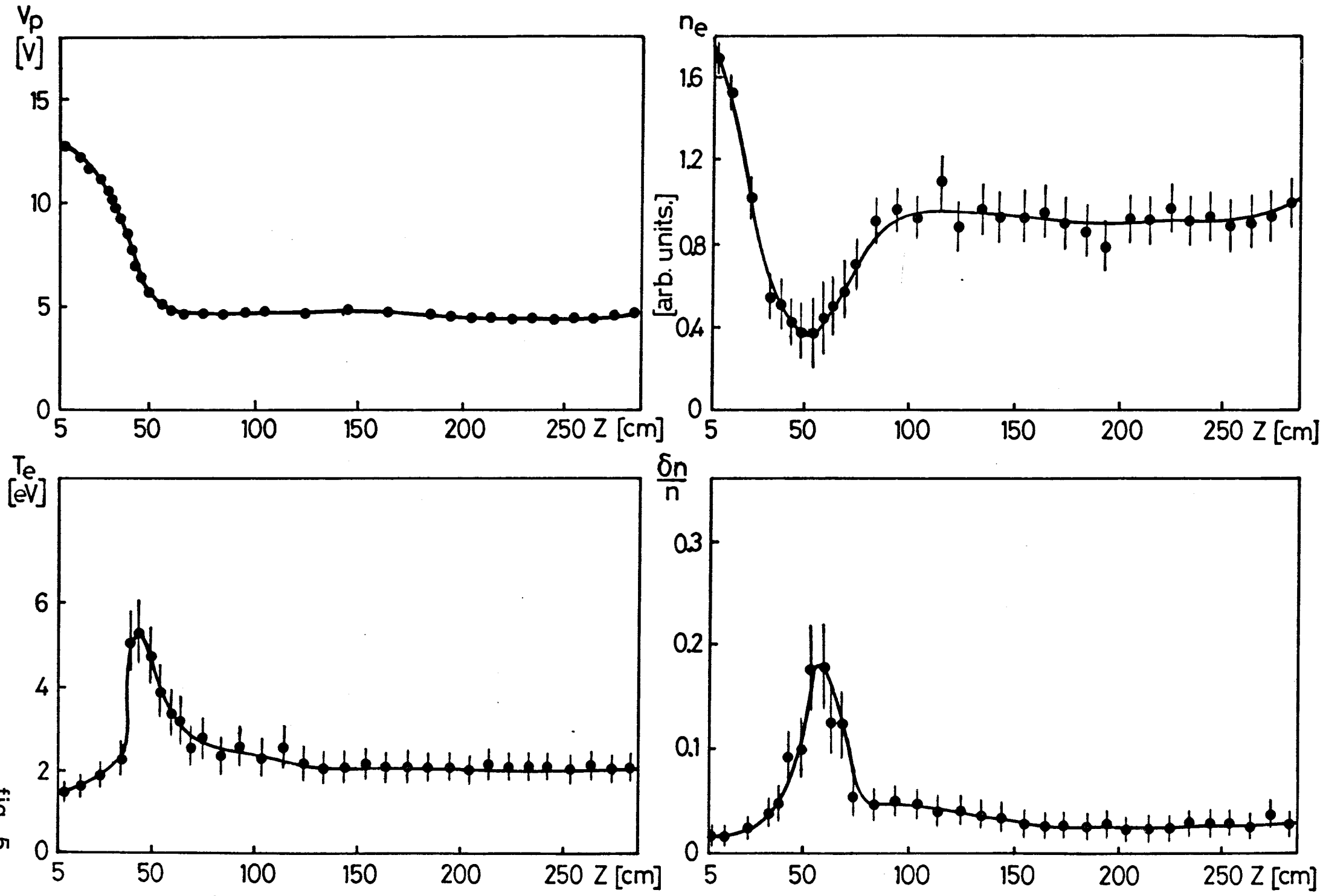
V_p [V]
15
10
5
0
5
50
100
150
200
250 Z [cm]
n_e
1.6
1.2
0.8
0.4
0
[arb. units.]
T_e [eV]
6
4
2
$\frac{\delta n}{n}$
0.3
0.2
0.1

fig. 5

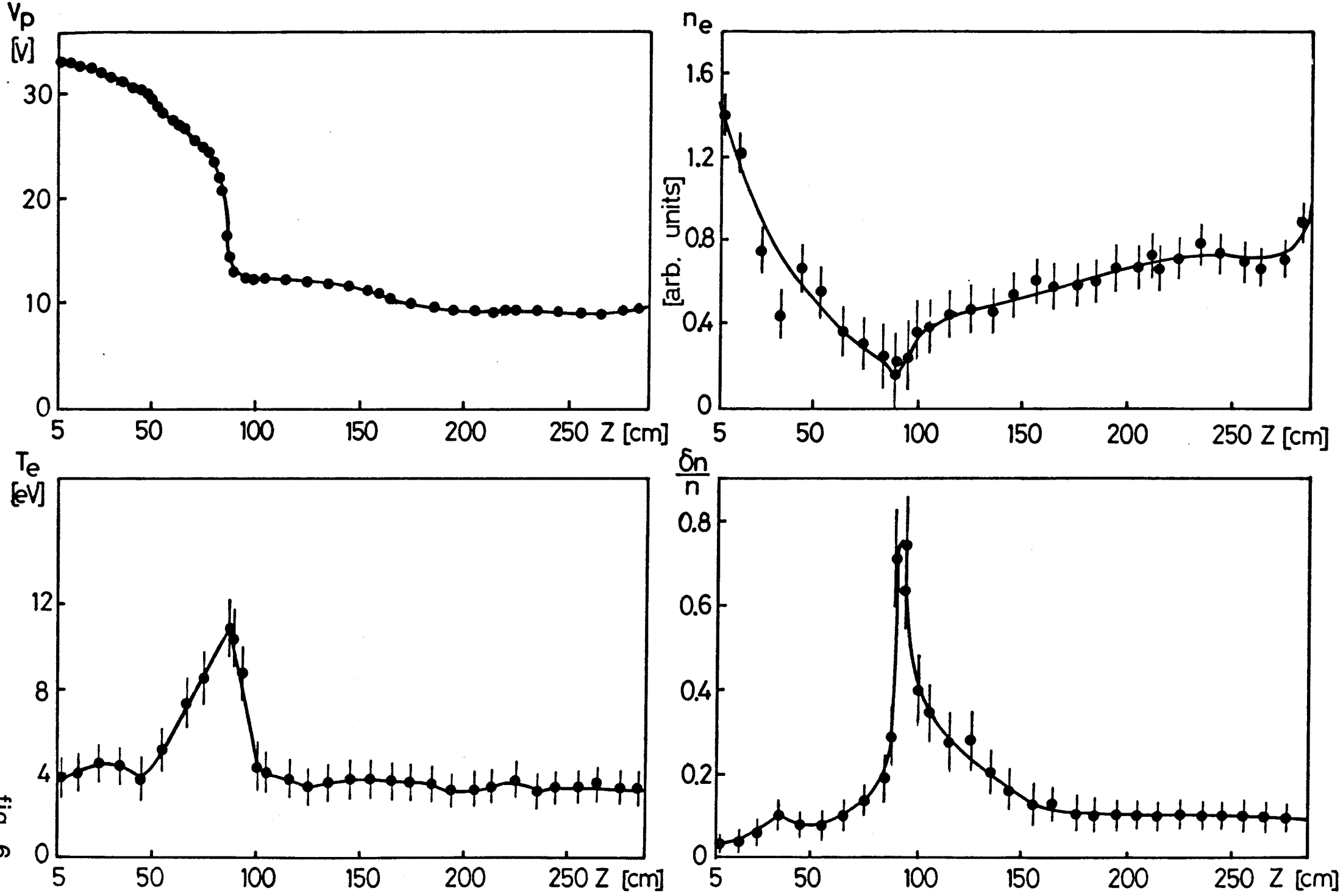
V_p [V]
30
20
10
0
5
50
100
150
200
250 Z [cm]
n_e
[arb. units]
1.6
1.2
0.8
0.4
0
T_e [eV]
12
8
4
$\frac{\delta n}{n}$
0.6
0.2

fig. 6

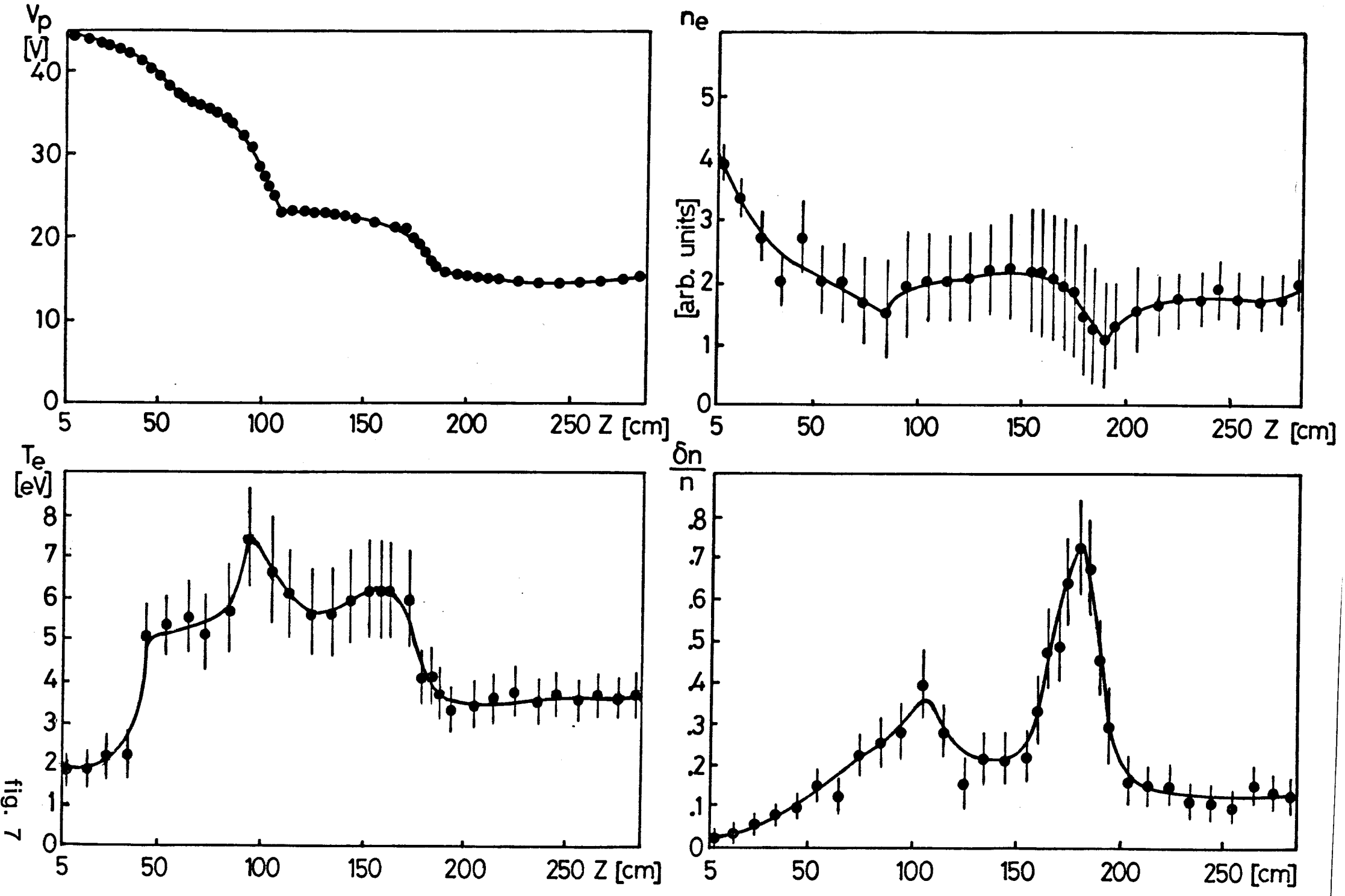
V_p [V]
40
30
20
10
0
5
50
100
150
200
250 Z [cm]
n_e
[arb. units]
5
4
3
2
1
0
5
50
100
150
200
250 Z [cm]
T_e [eV]
8
7
6
5
4
3
2
1
0
5
50
100
150
200
250 Z [cm]
$\frac{\delta n}{n}$
.8
.7
.6
.5
.4
.3
.2
.1
0
5
50
100
150
200
250 [cm]

fig. 7

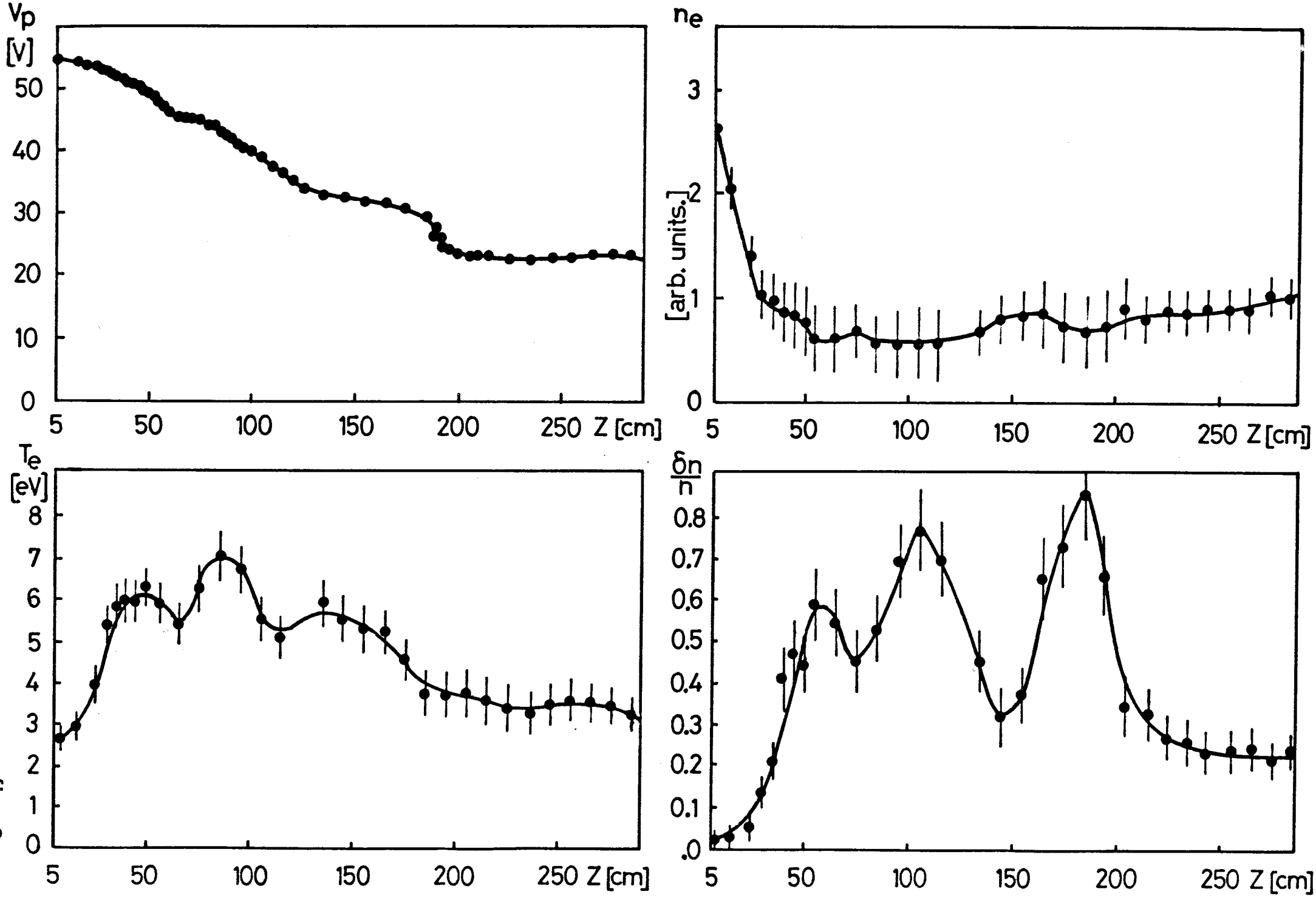
V_p [V]
50
40
30
20
10
0
5
50
100
150
200
250 Z [cm]
n_e
[arb. units.]
3
2
1
0
5
50
100
150
200
250 Z [cm]
T_e [eV]
8
7
6
5
4
3
2
1
0
5
50
100
150
200
250 Z [cm]
$\frac{\delta n}{n}$
0.8
0.7
0.6
0.5
0.4
0.3
0.2
0.1
.0
5
50
100
150
200
250 Z [cm]

fig. 8

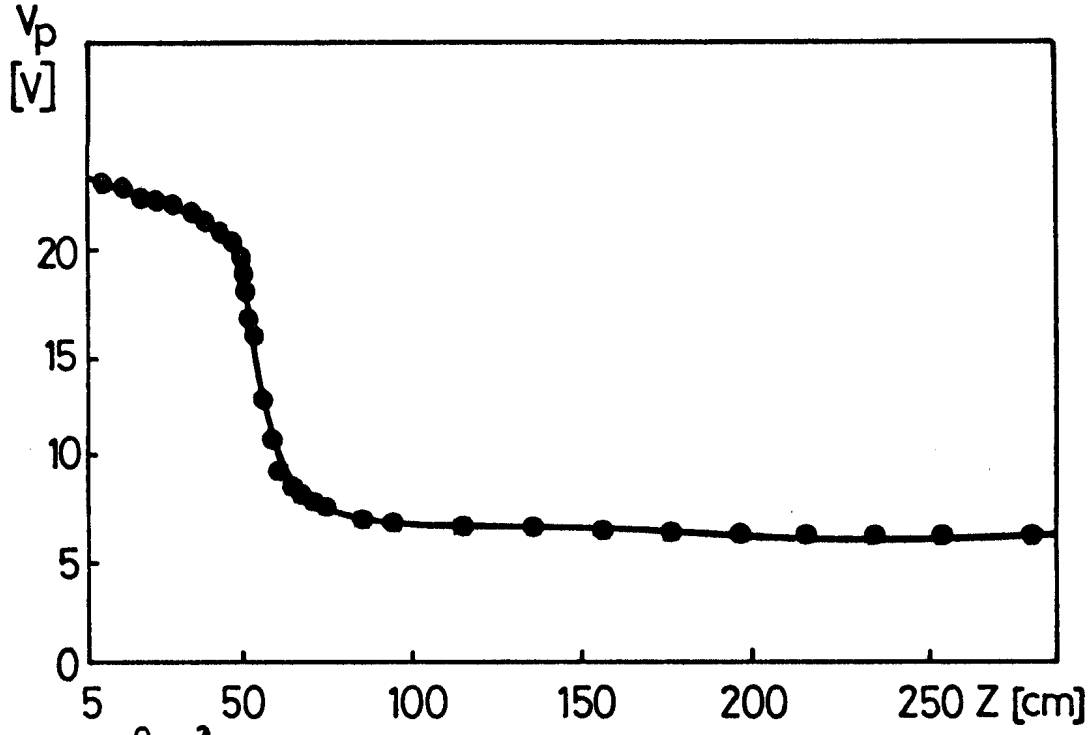
V_p [V]
20
15
10
5
0
5
50
100
150
200
250 Z [cm]

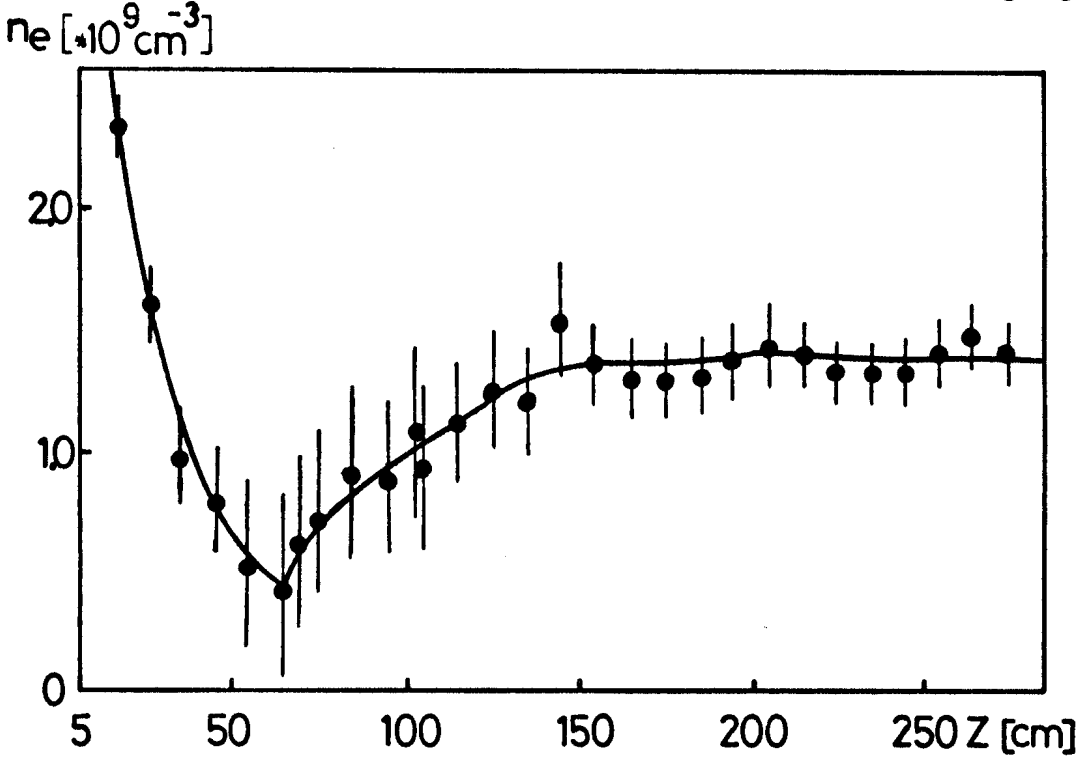
n_e [$*10^9 cm^{-3}$]
2.0
1.0
0
5
50
100
150
200
250 Z [cm]

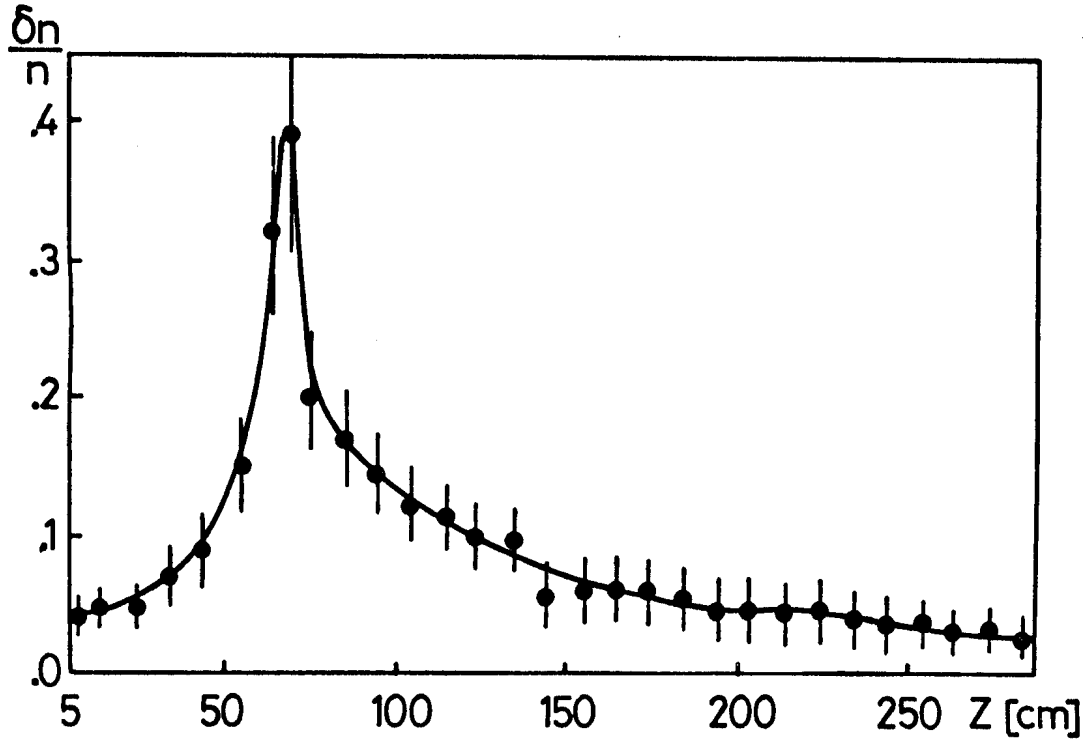
$\frac{\delta n}{n}$
.4
.3
.2
.1
.0
5
50
100
150
200
250 Z [cm]

fig. 9

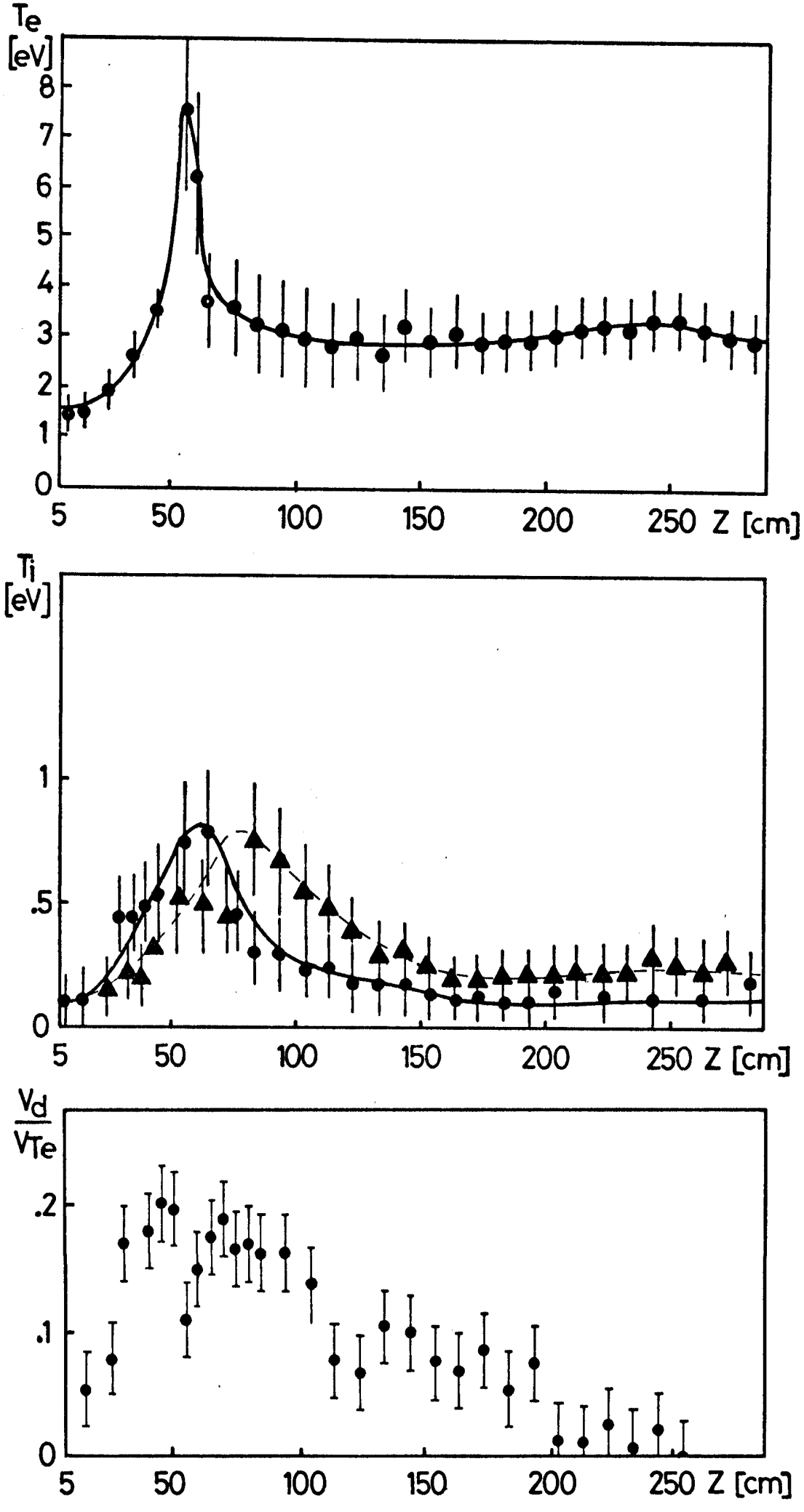
Te
[eV]
8
7
6
5
4
3
2
1
0
5
50
100
150
200
250 Z [cm]
Ti
[eV]
1
.5
0
5
50
100
150
200
250 Z [cm]
Vd
VTe
.2
.1
0
5
50
100
150
200
250 Z [cm]

fig. 10

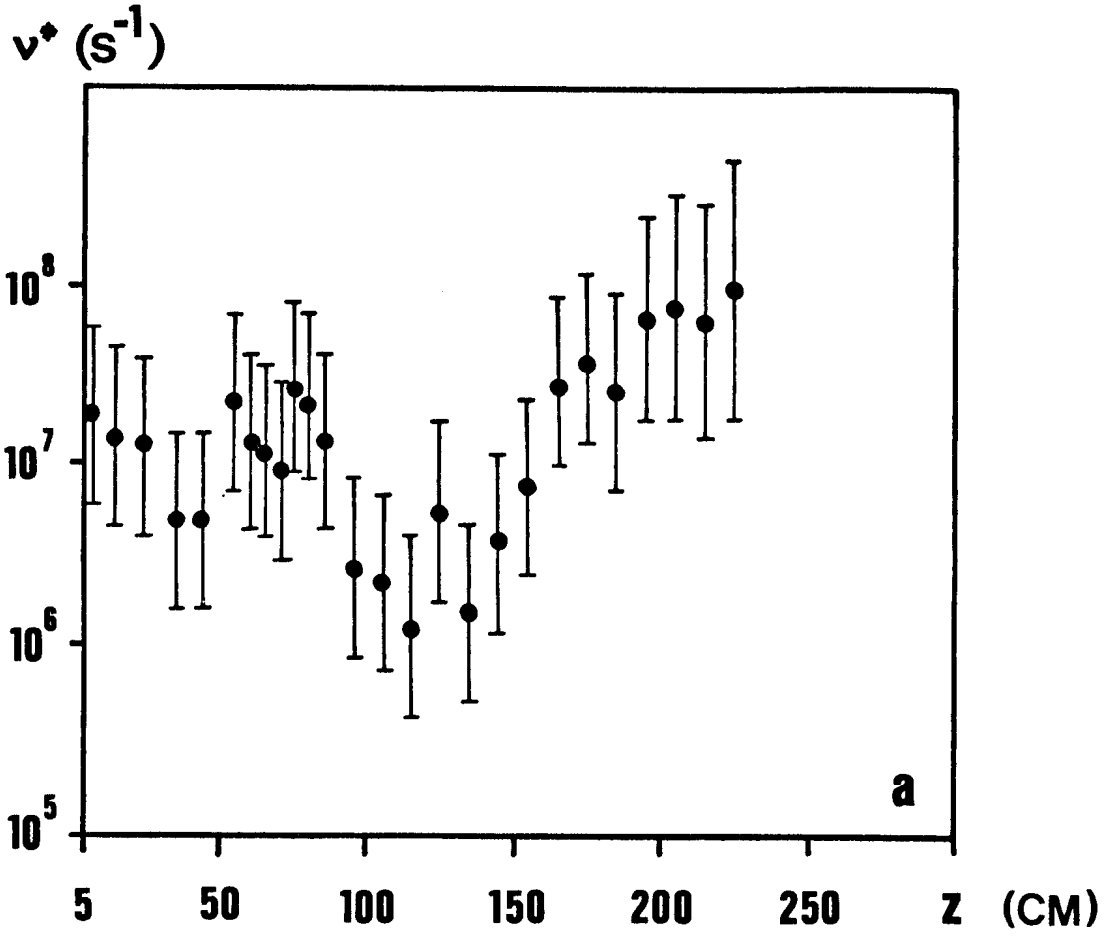
ν* (s-1)
10^8
10^7
10^6
10^5
a
5
50
100
150
200
250
z (CM)

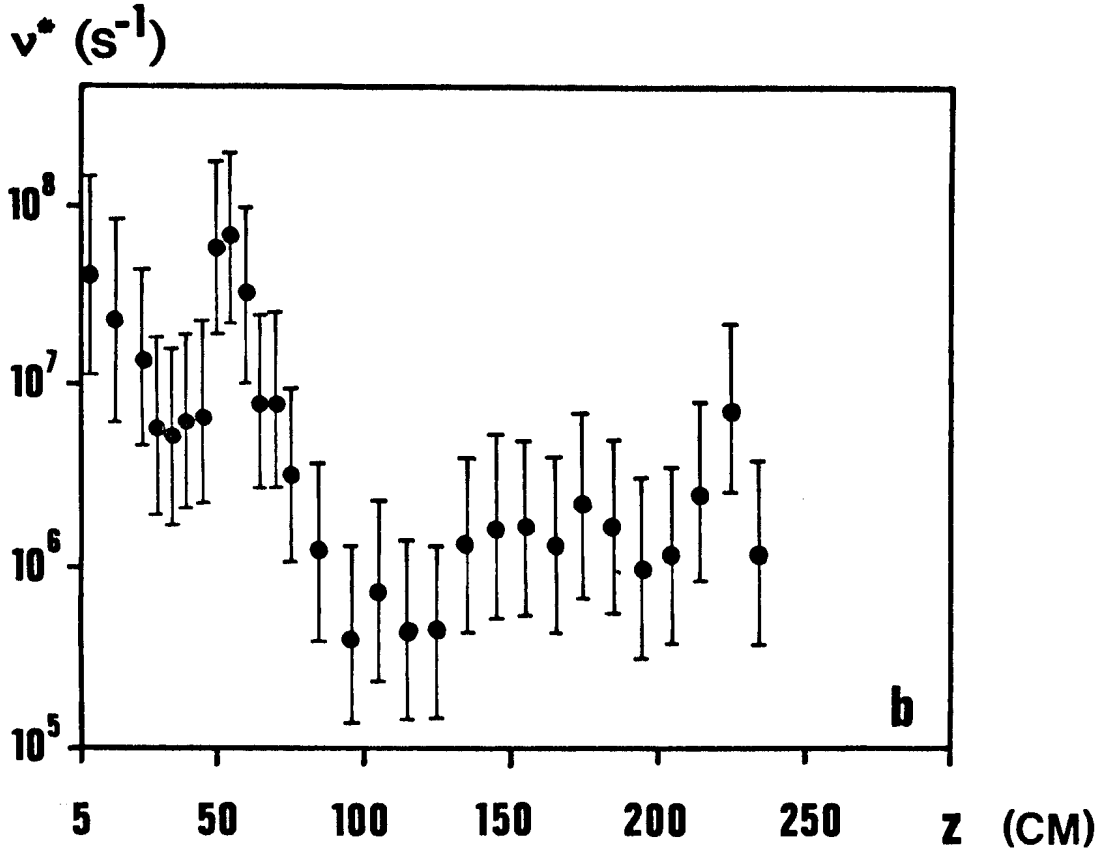
ν* (s-1)
10^8
10^7
10^6
10^5
b
5
50
100
150
200
250
z (CM)

fig. 11

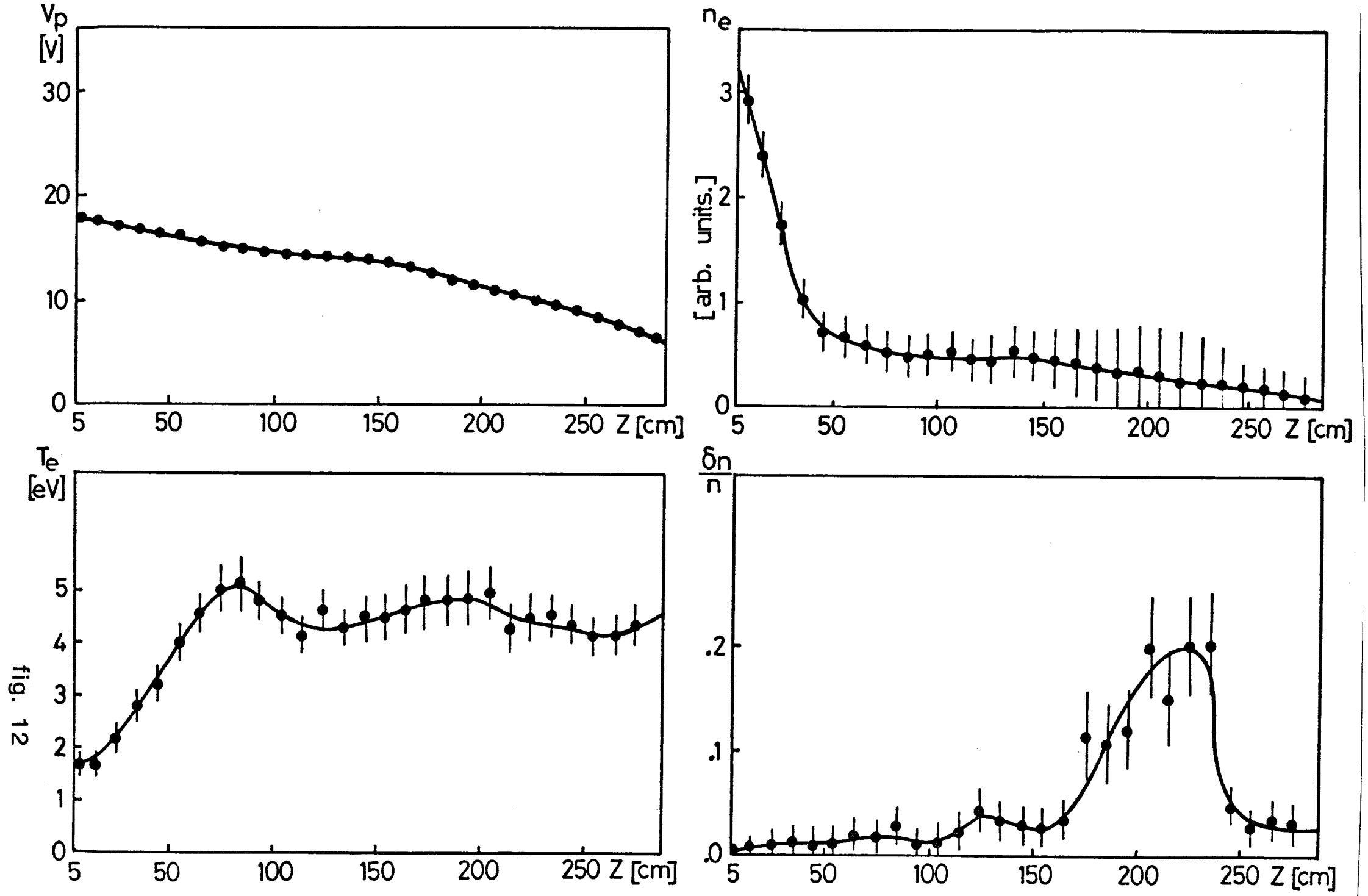
V_p [V]
30
20
10
0
5
50
100
150
200
250 Z [cm]
n_e
[arb. units.]
3
2
1
0
5
50
100
150
200
250 Z [cm]
T_e [eV]
5
4
3
2
1
0
5
50
100
150
200
250 Z [cm]
$\frac{\delta n}{n}$
.2
.1
.0
5
50
100
150
200
250 Z [cm]

fig. 12

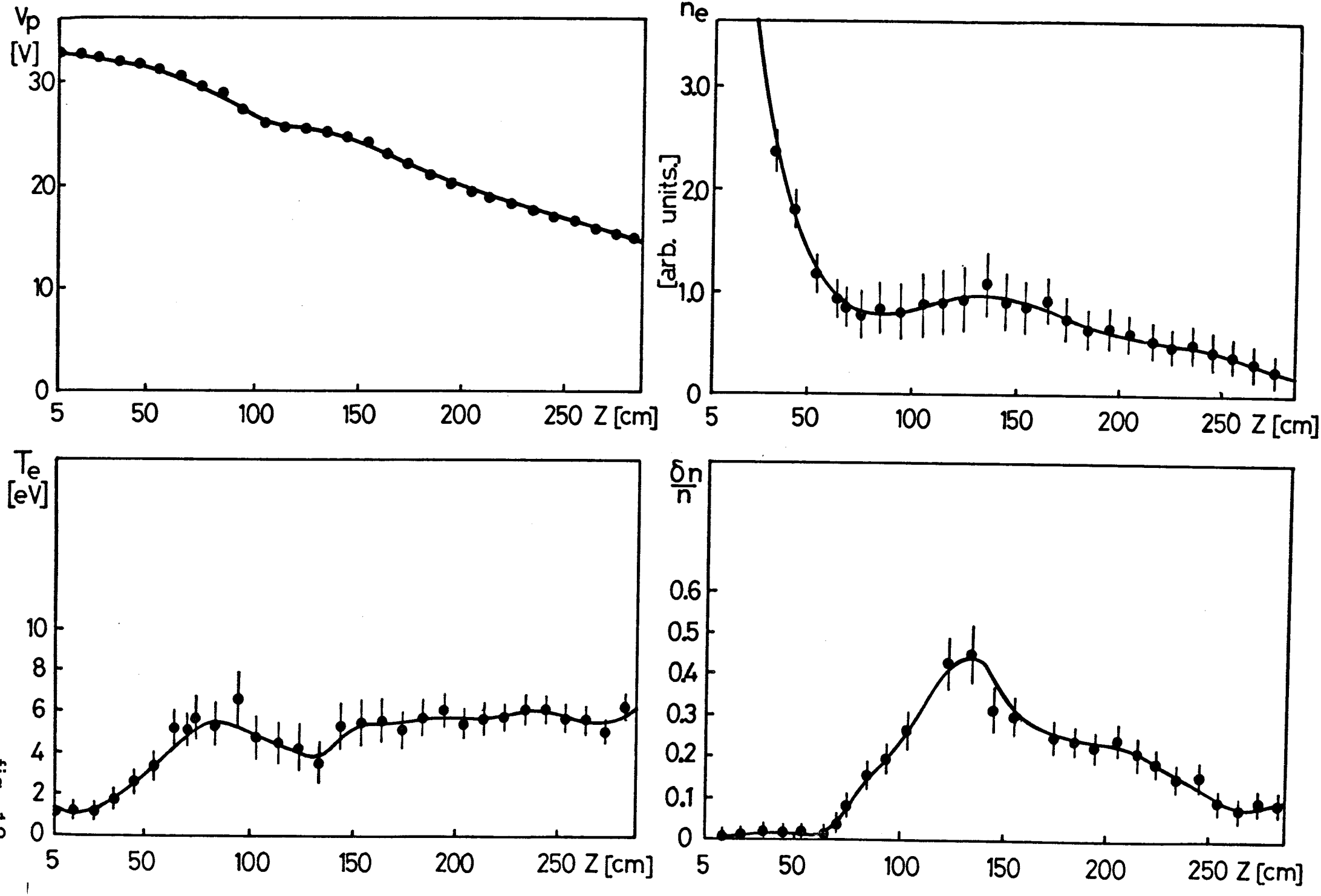
V_p [V]
30
20
10
0
5
50
100
150
200
250 Z [cm]
n_e
[arb. units]
3.0
2.0
1.0
0
T_e [eV]
10
8
6
4
2
0
$\frac{\delta n}{n}$
0.6
0.5
0.4
0.3
0.2
0.1

fig. 13

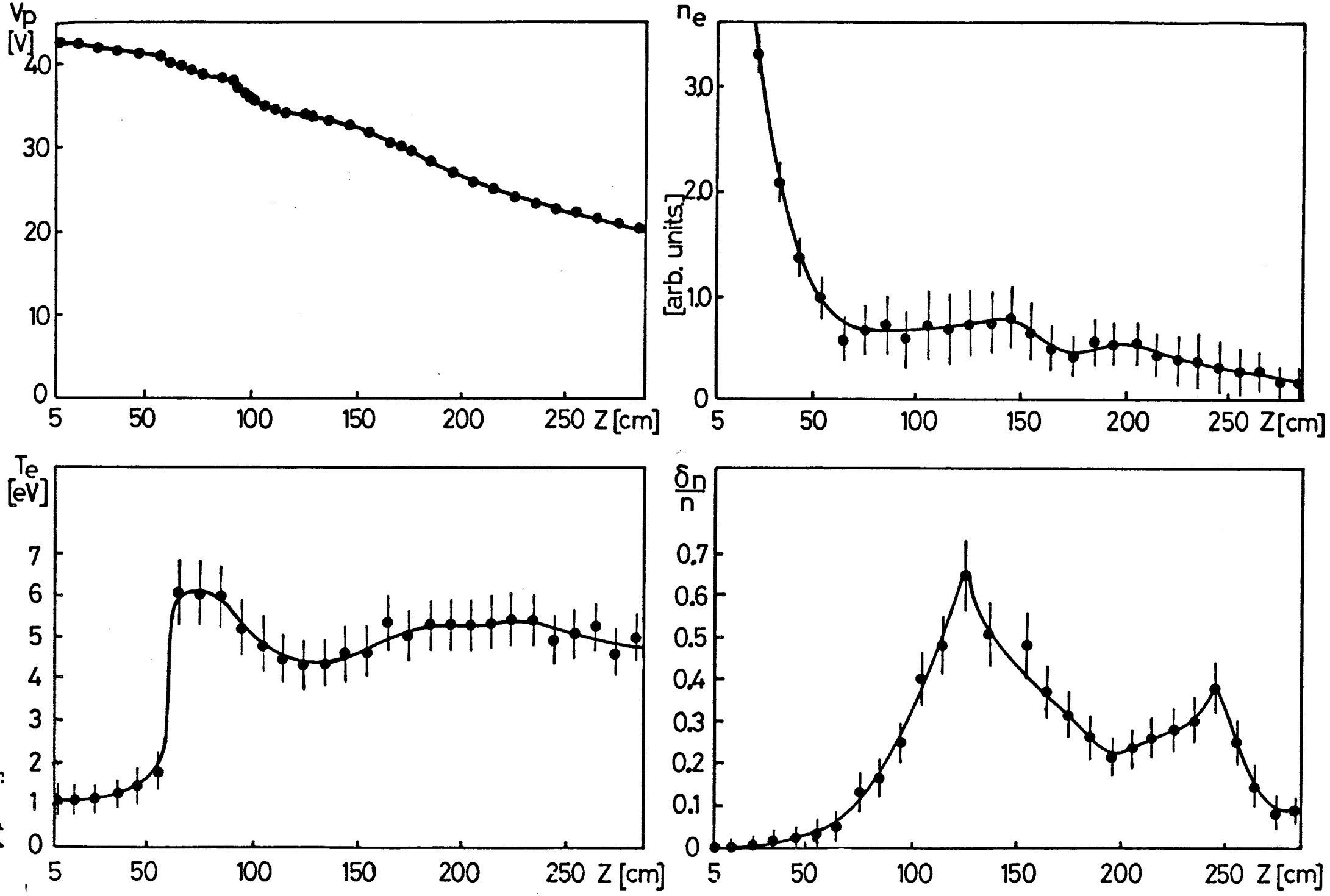
Vp
[V]
40
30
20
10
0
5
50
100
150
200
250 Z [cm]
n_e
3.0
2.0
1.0
0
[arb. units]
5
50
100
150
200
250 Z [cm]
Te
[eV]
7
6
5
4
3
2
1
0
5
50
100
150
200
250 Z [cm]
$\frac{\delta n}{n}$
0.7
0.6
0.5
0.4
0.3
0.2
0.1
0
5
50
100
150
200
250 Z [cm]

fig. 14

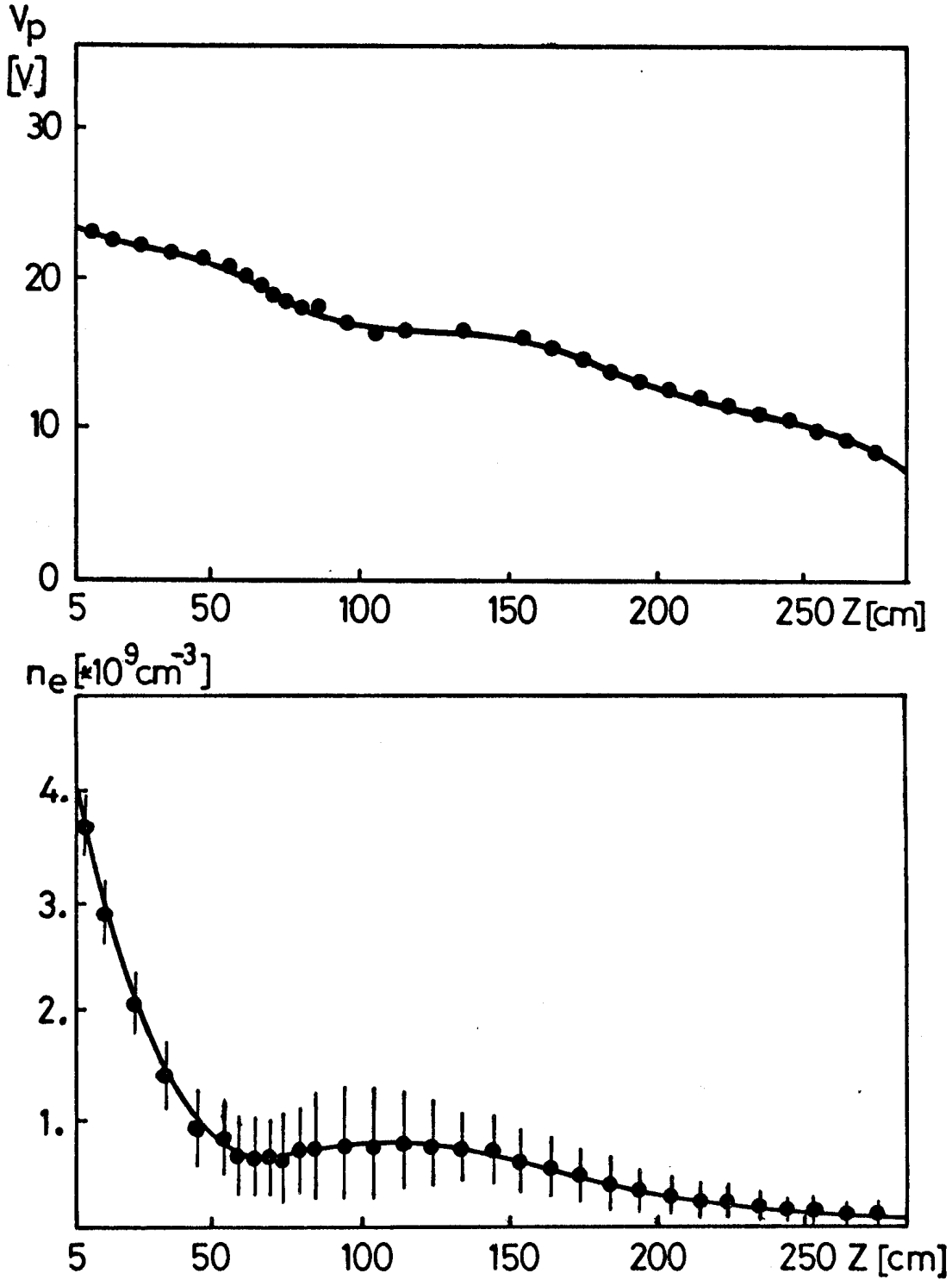
V_p [V]
30
20
10
0
5
50
100
150
200
250 Z [cm]

n_e [$*10^9 cm^{-3}$]
4.
3.
2.
1.
5
50
100
150
200
250 Z [cm]

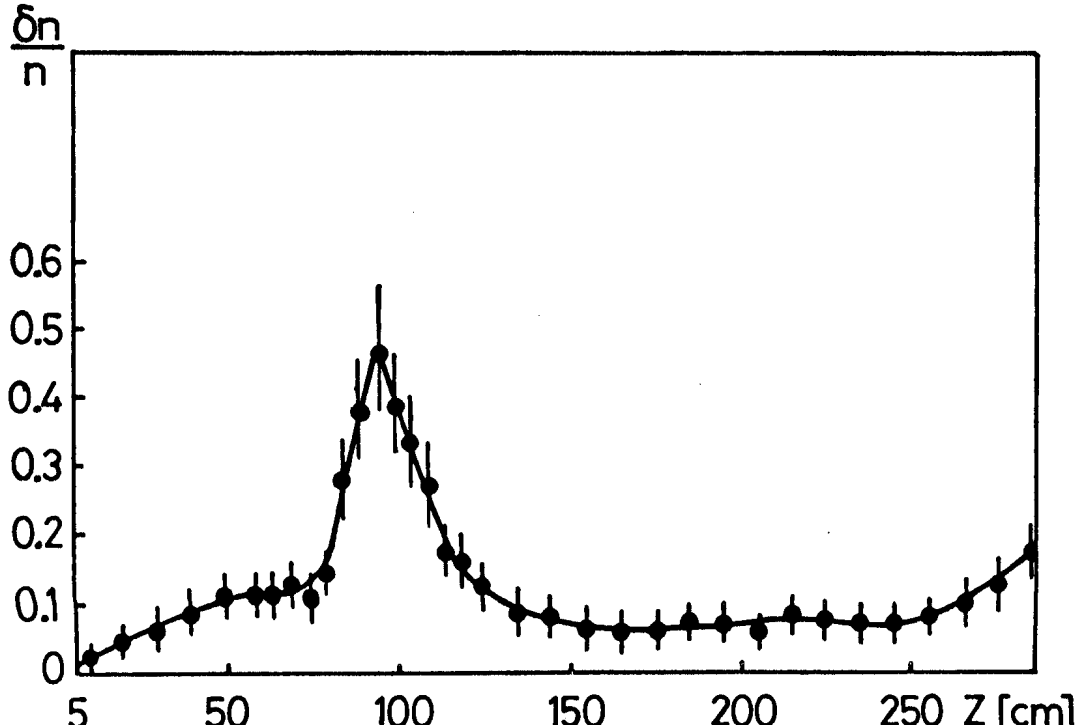
$\frac{\delta n}{n}$
0.6
0.5
0.4
0.3
0.2
0.1
0
5
50
100
150
200
250 Z [cm]

fig. 15

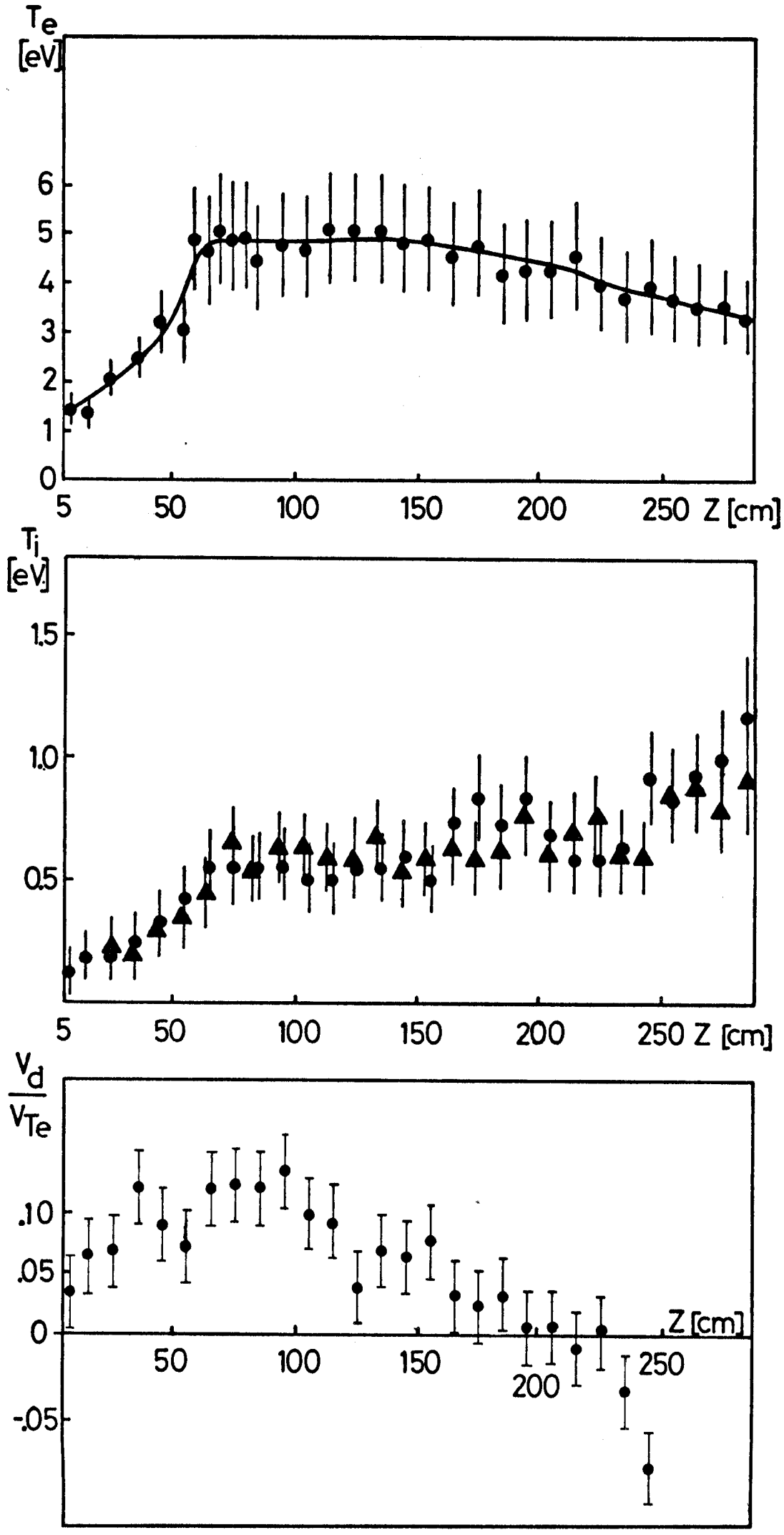
T_e [eV]
6
5
4
3
2
1
0
5
50
100
150
200
250 Z [cm]
T_i [eV]
1.5
1.0
0.5
5
50
100
150
200
250 Z [cm]
$\frac{V_d}{V_{Te}}$
.10
.05
0
-.05
50
100
150
200
250
Z [cm]

fig. 16

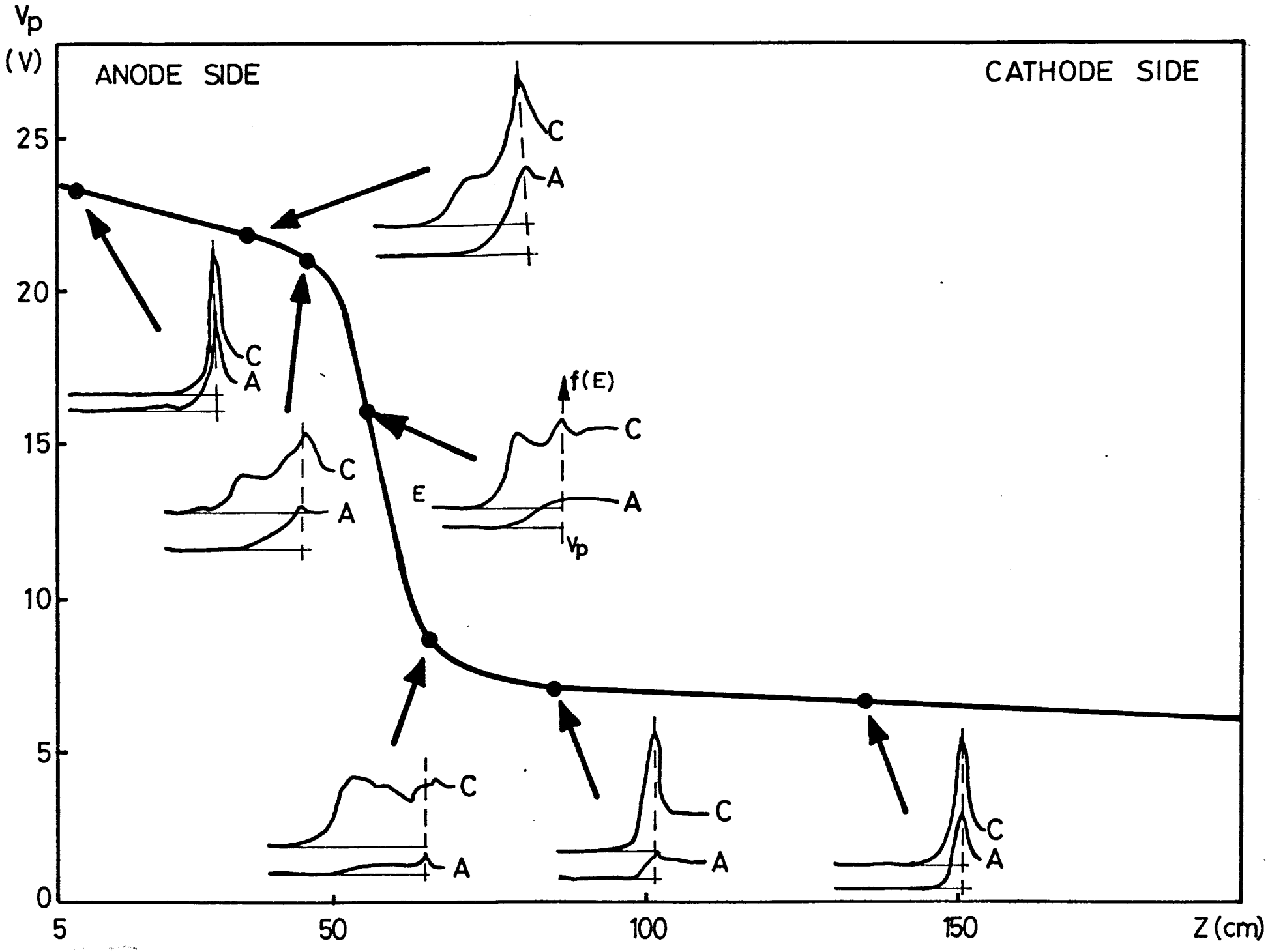
Vp
(V)
ANODE SIDE
CATHODE SIDE
25
20
15
10
5
0
5
50
100
150
Z (cm)
C
A
f(E)
E
Vp

fig. 17

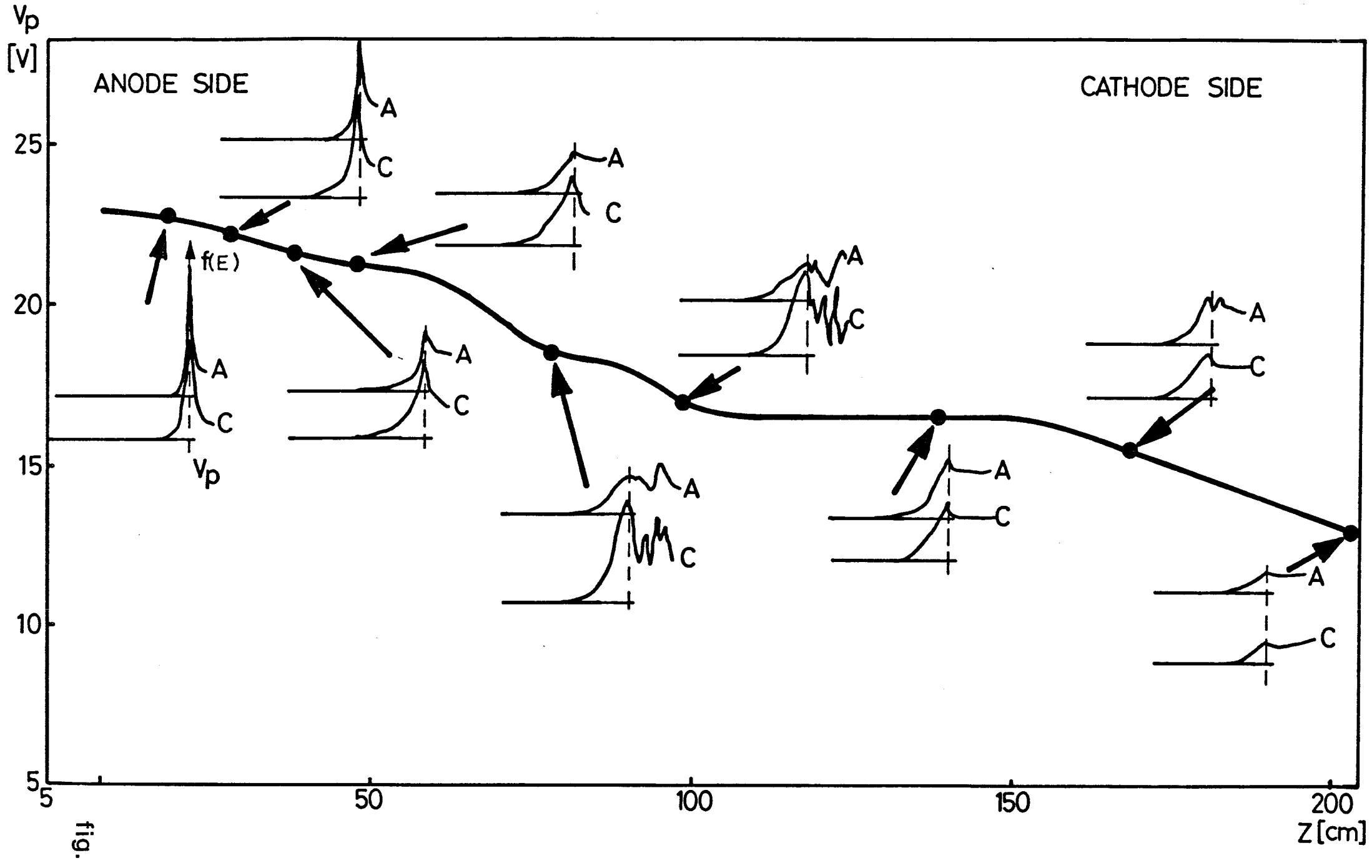
Vp
[V]
ANODE SIDE
CATHODE SIDE
25
20
15
10
5
5
50
100
150
200
Z [cm]
f(E)
Vp
A
C

fig. 18

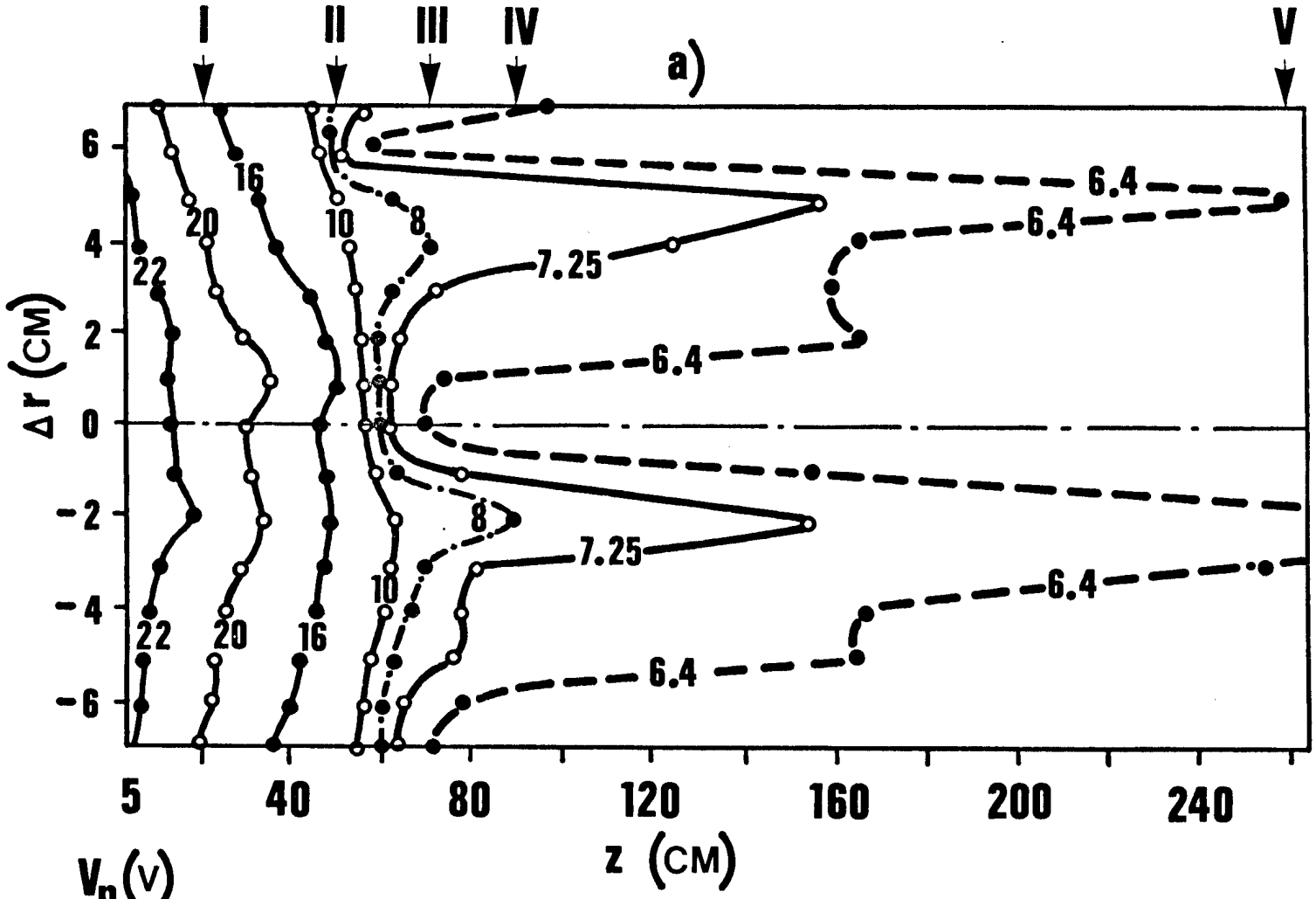
I
II
III
IV
V
a)
6.4
7.25
8
10
16
20
22
Δr (CM)
z (CM)
5
40
80
120
160
200
240

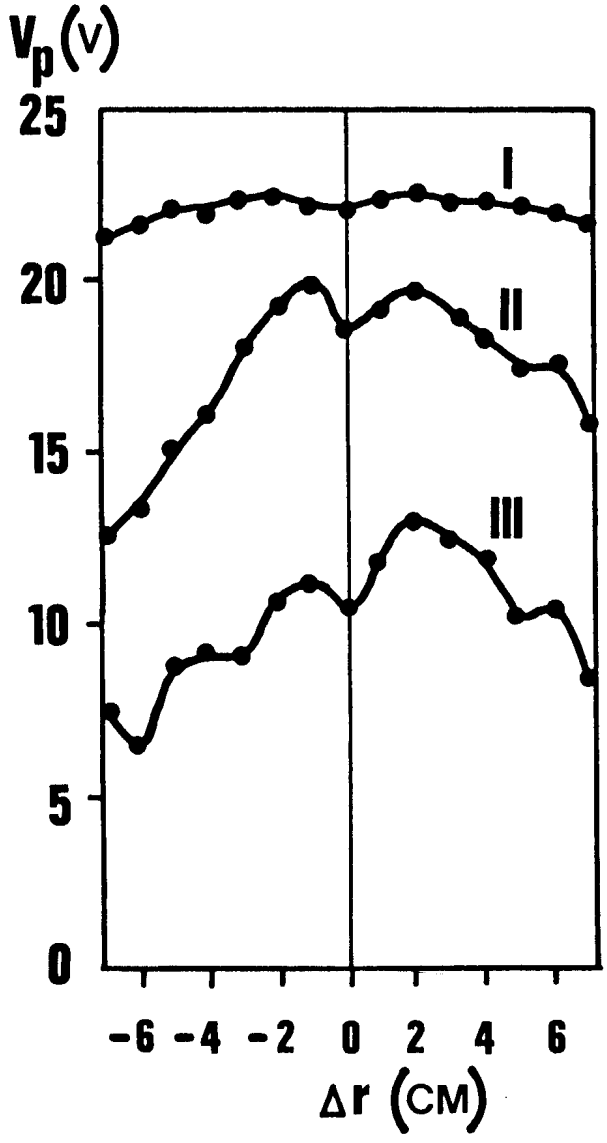
V_p (V)
I
II
III
Δr (CM)

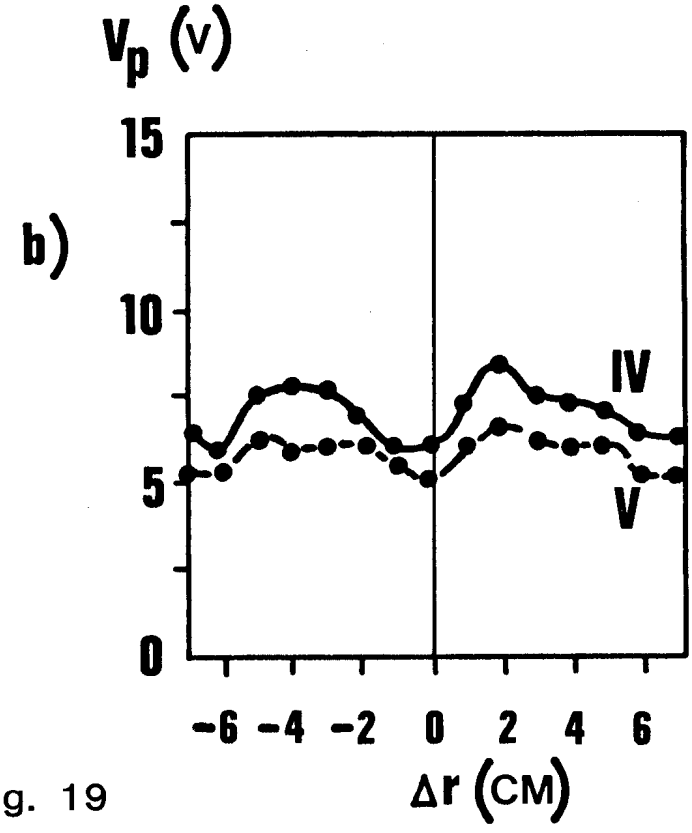
V_p (V)
b)
IV
V
Δr (CM)

fig. 19

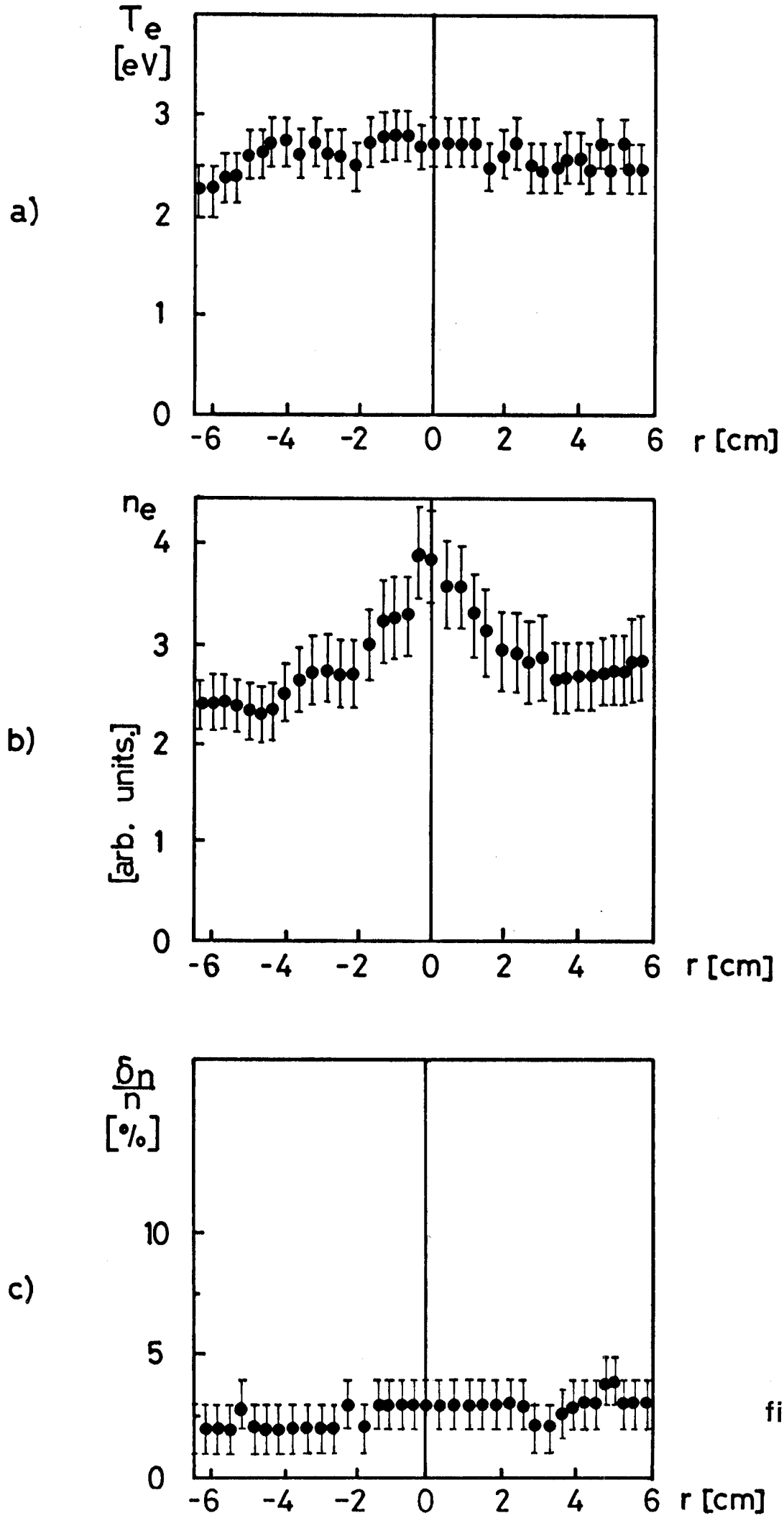
a)
T_e [eV]
3
2
1
0
-6 -4 -2 0 2 4 6 r [cm]
b)
n_e
4
3
2
1
0
[arb. units]
-6 -4 -2 0 2 4 6 r [cm]
c)
$\frac{\delta n}{n}$ [%]
10
5
0
-6 -4 -2 0 2 4 6 r [cm]

fig. 20

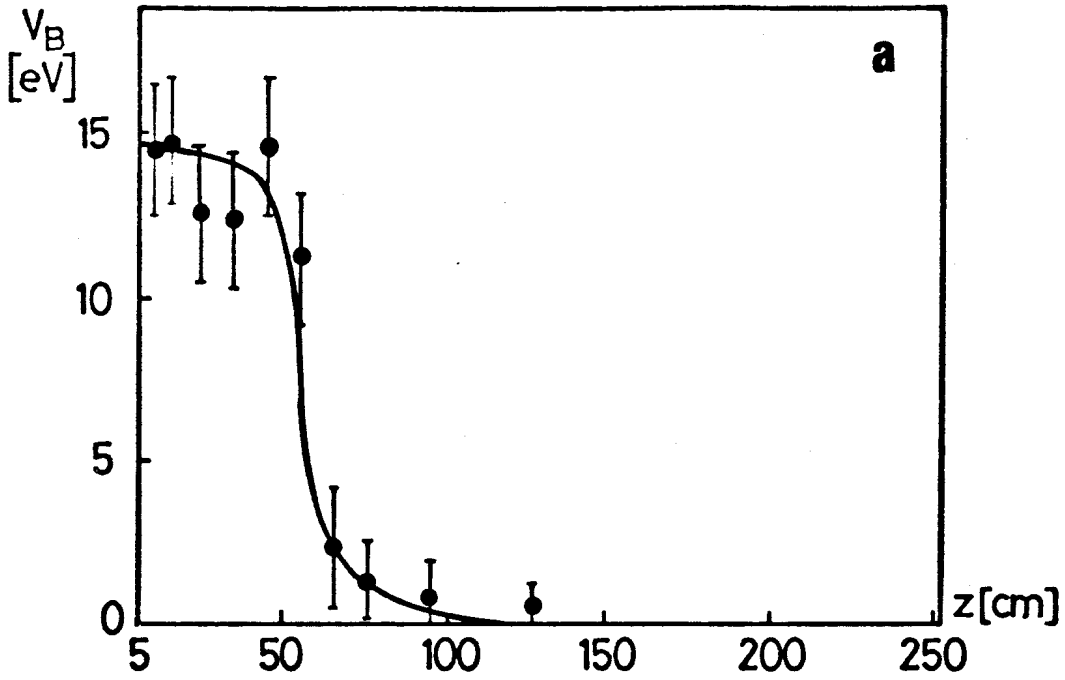
V_B [eV]
a
15
10
5
0
5
50
100
150
200
250
z[cm]

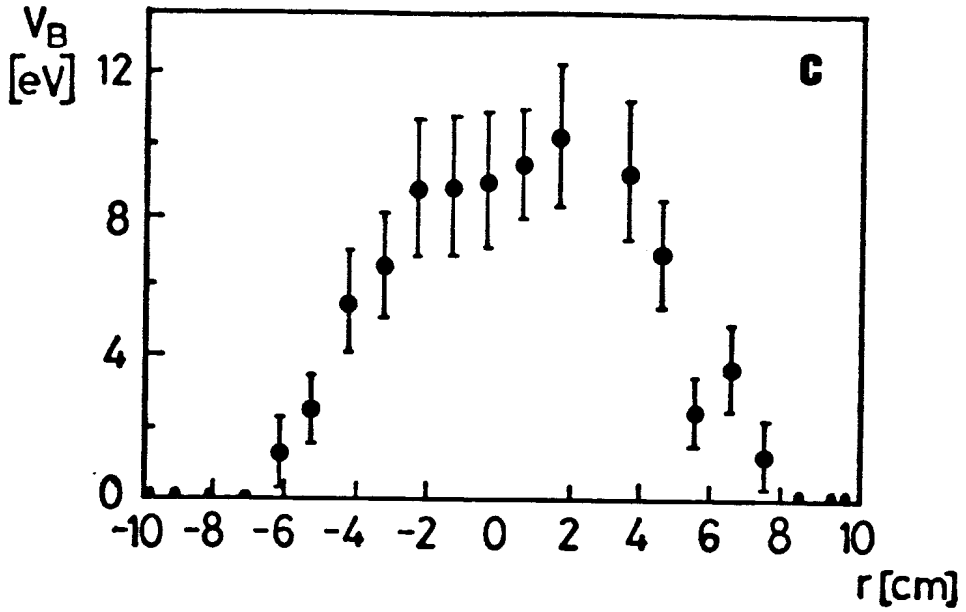
V_B [eV]
c
12
8
4
0
-10 -8 -6 -4 -2 0 2 4 6 8 10
r [cm]

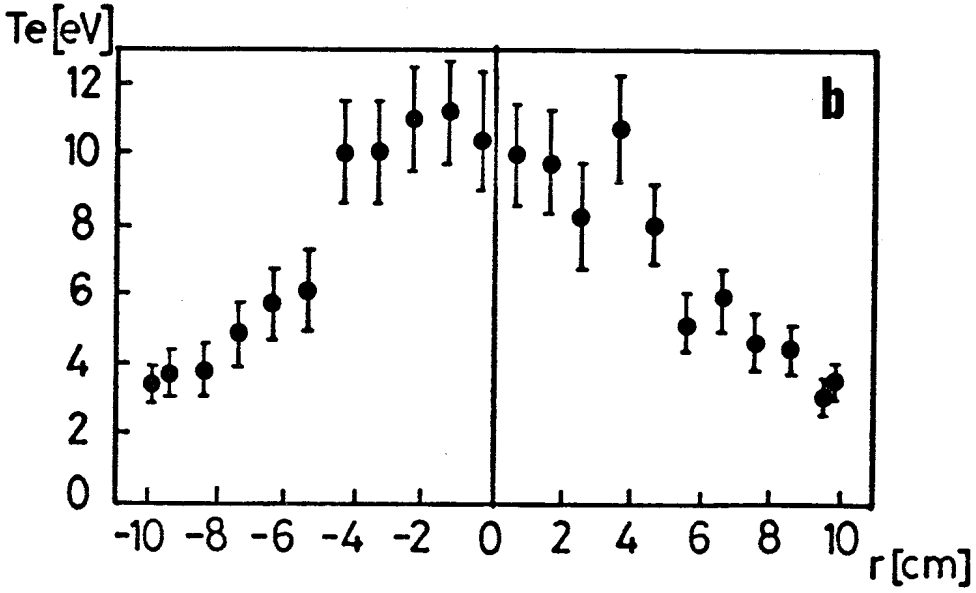
Te [eV]
b
12
10
8
6
4
2
0
-10 -8 -6 -4 -2 0 2 4 6 8 10
r [cm]

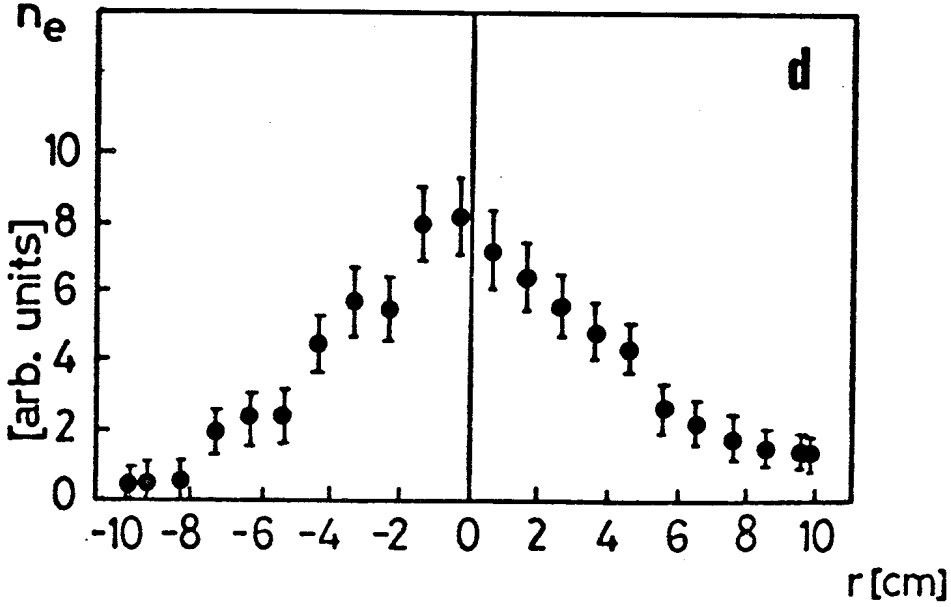
n_e
d
[arb. units]
10
8
6
4
2
0
-10 -8 -6 -4 -2 0 2 4 6 8 10
r [cm]

fig. 21